Rapid X-ray Photoreduction of Dimetal-Oxygen Cofactors in Ribonucleotide Reductase[S]

Kajsa G. V. Sigfridsson[‡1], Petko Chernev[‡], Nils Leidel[‡], Ana Popović-Bijelić[§2], Astrid Gräslund[§3], and Michael Haumann[‡4]

From the [§]Department of Biochemistry and Biophysics, Stockholm University, 10691 Stockholm, Sweden and the [‡]Free University Berlin, Institute of Experimental Physics, 14195 Berlin, Germany

Background: Typical FeFe and MnFe cofactors bind to numerous enzymes such as ribonucleotide reductases. Crystallographic data suggest x-ray photoreduction (XPR) effects.

Results: Rapid XPR-induced cofactor changes were monitored using time-resolved x-ray absorption spectroscopy.

Conclusion: The XPR-induced cofactor states differ significantly from the native configurations, but comply with crystallographic structures.

Significance: Structure determination for high-valent dimetal-oxygen cofactors requires free electron-laser protein crystallography combined with x-ray spectroscopy.

Prototypic dinuclear metal cofactors with varying metallation constitute a class of O_2-activating catalysts in numerous enzymes such as ribonucleotide reductase. Reliable structures are required to unravel the reaction mechanisms. However, protein crystallography data may be compromised by x-ray photoreduction (XRP). We studied XPR of Fe(III)Fe(III) and Mn(III)-Fe(III) sites in the R2 subunit of *Chlamydia trachomatis* ribonucleotide reductase using x-ray absorption spectroscopy. Rapid and biphasic x-ray photoreduction kinetics at 20 and 80 K for both cofactor types suggested sequential formation of (III,II) and (II,II) species and similar redox potentials of iron and manganese sites. Comparing with typical x-ray doses in crystallography implies that (II,II) states are reached in <1 s in such studies. First-sphere metal coordination and metal-metal distances differed after chemical reduction at room temperature and after XPR at cryogenic temperatures, as corroborated by model structures from density functional theory calculations. The inter-metal distances in the XPR-induced (II,II) states, however, are similar to R2 crystal structures. Therefore, crystal data of initially oxidized R2-type proteins mostly contain photoreduced (II,II) cofactors, which deviate from the native structures functional in O_2 activation, explaining observed variable metal ligation motifs. This situation may be remedied by novel femtosecond free electron-laser protein crystallography techniques.

Dinuclear transition-metal cofactors play important roles in small molecule conversions by a broad range of biological enzymes. A prominent example are the prototypic so-called dimetal-oxygen cofactors, which are found, for example, in ribonucleotide reductases (RNRs)[5] (1–3), methane monooxygenases (4, 5), and in various other oxidases (6–8). RNRs are essential for DNA synthesis in all organisms (9). In these enzymes, the metal cofactor is located in the R2 subunit, whereas the R1 subunit houses the active site of ribonucleotide reduction. In the classical R2 of *Escherichia coli* class-Ia RNR, two iron atoms form the cofactor, which are bound to the protein by the amino acid side chains of two histidine residues, three glutamates, and one aspartate, in a highly conserved binding motif (10, 11).

The metal cofactor in R2 proteins functions in dioxygen (O_2) reduction (12, 13). Activation of the enzymes is achieved by O_2 reduction at the initially divalent metal ions. Thereby the O-atoms become incorporated for example, as metal-bridging μO or μOH species (12–14) so that a high-valent Fe(IV)Fe(III) site (intermediate *X*) is formed (15–17). Subsequent oxidation of a nearby tyrosine residue to a radical (Y[•]) leaves the cofactor in an Fe(III)Fe(III) state. The catalytic cycle starts with the generation of a cysteine radical at the ribonucleotide binding site in R1 via long-range proton-coupled electron transfer to Y[•], initiating ribonucleotide reduction, in the course of which Y[•] is restored by reverse ET for further turnover (18–23).

Recently, a new class-Ic RNR has been described in the human pathogenic bacterium *Chlamydia trachomatis* (*Ct*), in which a hetero-dinuclear MnFe cofactor is assembled instead of an FeFe site and furthermore, the radical-forming tyrosine is replaced by a redox-inert phenylalanine (Phe-127) (24–27). Extensive investigations on the *Ct* enzyme have revealed that a Mn(IV)Fe(III) site, as formed after O_2 reduction at divalent

---

manganese and iron ions, is the target of the proton-coupled electron transfer from R1 (25–30). Also in CtR2 under certain conditions an FeFe cofactor can be incorporated, but shows significantly lower activity (31, 32). Similar MnFe sites meanwhile have been found in a number of related enzymes (7, 8, 33–36) and in addition, MnMn cofactors were described in the tyrosine-radical forming class-Ib RNRs (37–39). An important common feature of all three types of cofactors is the participation of high-valent intermediates, for example, M(III)M(III) and M(IV)M(III), in the catalytic reactions (25, 28, 35, 36).

The Protein Database was used for structures. Most R2 structures are for FeFe- or MnMn-containing proteins. Only very recently, three structures have been reported for CtR2 including a MnFe cofactor (41, 42). In previous studies (see Refs. 29 and 30), we have surveyed the R2 structures. In none of the structures did the apparent mean metal oxidation state exceed ~2.5 and the average value was close to 2, suggesting the predominance of M(III)M(II) and Mn(II)M(II) sites. The latter holds true also for structures that have been obtained for initially oxidized R2 proteins. In addition, considerable observed variability in metal coordination by oxygen species and amino acid groups is unexplained on a functional basis. Important structural parameters, such as the metal-metal distance, which is determined, *e.g.* by the type of metal-bridging oxide species (4, 30, 43, 44), are not correlated to the ligation environment or to the increasing crystallographic resolution over the last 20 years. Typical metal(II)-ligand bond lengths are often observed (29, 30).

These observations suggest that the metal sites in the crystal structures in fact do not correspond to high-valent states (29, 30). The likely reason for this is x-ray photoreduction (XPR) of initially high-valent cofactors during diffraction data collection (29, 30, 45). However, for well founded attributions, for example, on the O_2-activation process, reliable structural information is also required for the high-valent cofactors.

X-ray irradiation induced modifications are a long-known problem in protein crystallography (46–49). XPR of metal cofactors often occurs at x-ray doses that are orders of magnitudes lower than used in x-ray crystallography causing radiation damage of the protein matrix (50–62). XPR therefore has even been used to study reduced states of metal centers (51–53, 56). However, because of a limited, but significant mobility of atoms in proteins at the cryogenic temperatures (around 100 K) usually employed in crystallography, XPR-induced and native structures of cofactors in reduced states may be expected to be different (58, 60).

By x-ray absorption spectroscopy (XAS), structural (metal-ligand bond lengths, metal-metal distances) and electronic (oxidation state) parameters also for high-valent metal sites can be determined (63–65) and furthermore, this technique allows studies of the XPR kinetics (58–60, 66). Using XAS, for CtR2 we have shown previously that under high-intensity x-ray irradiation the Mn(IV)Fe(III) cofactor becomes reduced by XPR within seconds to minutes even at 20 K (30). However, quantitative relationships between XPR-induced structural changes and metal oxidation states so far have not been obtained for the dimetal-oxygen cofactors. This is necessary to reconcile the site configurations in the crystal data with deviating structural features, for example, usually much shorter metal-metal distances, as determined by XAS (29, 30, 66–68). In principle, this would allow for the reversion of modifications due to XPR in the crystal structures *in silico*, using quantum chemical calculations (64, 69, 70), to obtain improved models of the high-valent sites.

In the present investigation, we used XAS to monitor XPR in CtR2 initially containing Fe(III)Fe(III) or Mn(III)Fe(III) cofactors at cryogenic temperatures. The XPR kinetics were determined by time-resolved XANES measurements and the structural changes, as derived from EXAFS analysis, were put in relationship to the XPR-induced metal oxidation states. Rapid XPR was observed for both cofactor types. This gave rise to site configurations, which differ from the ones in the native oxidized or reduced CtR2 proteins, but are in agreement with crystallographic data.

MATERIALS AND METHODS

Protein Sample Preparation—Recombinant Ct R2 protein was overexpressed in *E. coli* and R2 protein was purified and concentrated as described previously (see Refs. 29 and 30 and references therein). R2 protein containing an FeFe cofactor was obtained without addition of metal ions to the TB growth medium. R2 protein containing predominantly a MnFe cofactor was obtained by the addition of 30 μM $MnCl_2$ to the LB medium (iron concentration 8 μM) after induction with isopropyl isopropyl-β-D-thiogalactopyranoside. Reduction of R2 was achieved by the addition of 100 μM TCEP (Tris(2-carboxyethyl)phosphine hydrochloride) to the cell lysis buffer. R2 protein (monomer) concentrations were derived photometrically using an extinction coefficient at 280 nm of 57,750 M^{-1} cm^{-1} for Ct R2 (27). The following protein samples were prepared. (*a*) Oxidized MnFe R2 protein, as aerobically purified from cells grown in manganese-enriched medium, further on is denoted $CtR2_{MnFe}{}^{ox}$; (*b*) chemically reduced MnFe R2 is denoted $CtR2_{MnFe}{}^{red}$; (*c*) FeFe R2 protein, as aerobically purified from cells grown in TB medium (14 μM iron) (71), is denoted $CtR2_{FeFe}{}^{ox}$; and (*d*) chemically reduced FeFe R2 is denoted $CtR2_{FeFe}{}^{red}$. XPR studies were carried out on $CtR2_{MnFe}{}^{ox}$ and $CtR2_{FeFe}{}^{ox}$ samples and resulted in R2 states denoted $CtR2_{MnFe/FeFe}{}^{xi}$ (xi specifies the mean x-ray irradiation period in min, *i.e.* $CtR2_{FeFe}{}^{x90}$ for 90 min of x-ray exposure).

Metal Content Quantification—Metal contents of R2 samples were quantified by total-reflection x-ray fluorescence analysis (TXRF) (29, 30, 72) on a PicoFox spectrometer (Bruker) using a gallium metal standard (Sigma) and the respective R2 polypeptide concentrations.

X-ray Absorption Spectroscopy—XAS was performed at the SuperXAS beamline of the Swiss Light Source (SLS) at Paul Scherrer Institute (Villigen, Switzerland) using a double-crystal Si[111] monochromator. Higher harmonics were suppressed by a silicon mirror in grazing incidence mode. The synchrotron was operated in top-up mode at 400 mA ring current, providing constant x-ray flux at the sample position, which was attenuated by carbon foil absorbers in the beam when necessary. A rapid shutter in front of the I_0 ion chamber prevented x-ray irradiation of samples prior to the XAS scans. The spot size on the samples was ~0.2 mm (vertical) × ~1.0 mm (horizontal) as set by slits. Samples were positioned with micrometer precision

in the beam by moving the cryostat on a computer-controlled stage. Kα fluorescence-detected XAS spectra at the iron and manganese K-edges were collected using an energy-resolving 13-element germanium detector (Canberra), which was shielded by 3-μm chromium foil (Mn) or 6-μm manganese foil (iron) against scattered x-rays. Samples were held in a liquid-helium cryostat (Oxford). Detector dead time-corrected XAS spectra were averaged after energy calibration using an iron metal foil (iron) or a KMnO$_4$ powder sample (manganese) as energy standards (73, 74). XANES spectra were normalized and EXAFS oscillations were extracted as described previously (30). The duration of EXAFS scans up to a k value of 12.5 Å^{-1} was ~22 min; the scan duration up to the K-edge was ~1–2 min. EXAFS spectra were derived using E_0 values of 7112 eV (iron) and 6540 eV (manganese); E_0 was refined to 7120 ± 2 eV (iron) and 6547 ± 2 eV (manganese) in the least-squares simulations of unfiltered k^3-weighted spectra (in-house program SimX (75), phase functions were calculated by FEFF8 (76, 77), amplitude reduction factors, S_0^2, of 0.9 for iron and 0.85 for manganese). The error sum (R_F) was defined as described elsewhere (75). Fourier transforms (FTs) of EXAFS spectra were calculated using k values of 2–12 Å^{-1} and cos^2 windows extending over 10% at both k range ends. K-edge energies were determined at the 50% level of the normalized XANES. Time scans of the x-ray fluorescence were recorded at given monochromator energies at the K-edges to monitor XPR (60), using an acquisition period of 2 s/data point. Kinetic XPR data were simulated by sums of monoexponential functions.

Bond Valence Sum Calculations—BVS calculations (78) were done as previously described (29–30), using in-house software for the analysis of crystal structure files from the Protein Data-base, and included atoms within a radius of 2.7 Å around the metal ions. Given BVS values represent the average of calculations using R_0 values for metal(II) and metal(III) species (30).

Density Functional Theory Calculations (DFT)—Spin-unrestricted geometry optimizations and calculations of electronic parameters of structural models of the metal sites were performed using the ORCA program package (79) as described previously (30, 80). Geometry optimizations involved the BP86 exchange-correlation functional (81) with a triple-ζ valence (TZVP) basis set (82). One set of polarization functions was used for all atoms. The resolution of identity approximation was used with the auxiliary TZV/J Coulomb fitting basis set (83) and a dielectric constant of $\epsilon = 4$ in a COSMO solvation model (84). To derive the correct spin coupling of the two metal atoms, broken symmetry formalism using the flip-spin technique as implemented in ORCA (85, 86) was applied as described before (30). The initial geometry optimizations of (III,III) cofactors were based on crystal structure PDB code 1SYY of wild type *Ct* FeFe R2. For further restrictions in the DFT calculations see the "Results."

RESULTS

Properties of Cofactors in CtR2 Crystals—Two crystal structures of the wild type *Ct*R2$_{MnFe}$ protein have been published (24, 32, 41, 42). Earlier structures of *Ct*R2 proteins produced in *E. coli* without addition of or reconstitution with manganese should relate to *Ct*R2$_{FeFe}$ proteins (wt and the F127Y mutant)
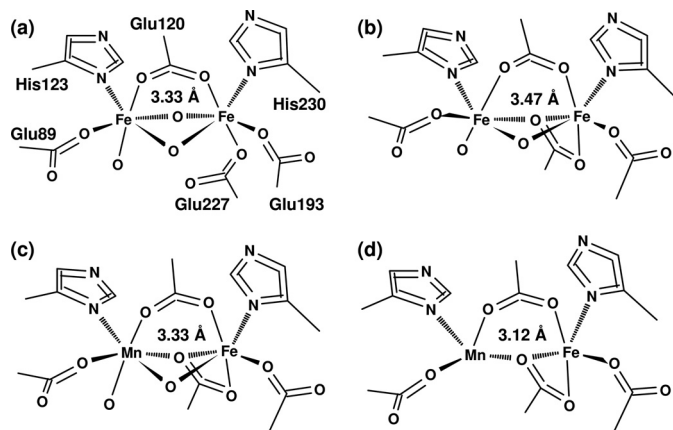
FIGURE 1. **Crystal structures of FeFe and MnFe cofactors in *Ct*R2.** The PDB entry numbers are shown (resolution and reference in parentheses): *a*, 1SYY (1.70 Å (24)); *b*, 2ANI (2.00 Å (25)); *c*, 4D8F (2.200 Å (42)); *d*, 4D8G (1.75 Å (42)). For *c* and *d*, one example of the 4 structures in the files is shown. The given metal-metal distances represent the mean values, the distance error may be on the order of ~0.2 Å. Note varying metal bridging oxides and structural changes at Glu-227. 2ANI (*b*) corresponds to the F127Y mutant. The following mean BVS values for Fe1,Fe2 or Mn,Fe (numbers of ligands in parentheses) were obtained from the structures: *a*, 2.3,2.4 (6,6); *b*, 2.7,4.7 (6,6); *c*, 1.6,1.1 (4.5,5); *d*, 2.4,2.1 (6,6).

(24, 32, 41, 42). The structures were initially obtained using oxidized R2, and were expected to contain mainly Fe(III)Fe(III) or Mn(III)/(IV)Fe(III) cofactors. All structures show different coordination motifs of the metal ions, in particular with respect to metal-bridging oxides and orientation of the carboxylate group of Glu-227 (Fig. 1). BVS calculations reveal apparent oxidation states, which are close to the divalent level even for the 6-coordinated metal ions (Fig. 1, see legend); the average metal-ligand bond lengths thus are in the range for Mn(II) and Fe(II) species.

The metal-metal distances span about 3.07–3.47 Å (Fig. 1) and are seemingly unrelated to the metal coordination. The coordinate error may be expected to be on the order of at least 10% of the crystallographic resolution (87). This means that the metal-metal distances in the *Ct*R2 structures at a resolution of ~2 Å may be considered as equal within error limits. These distances are within the range of metal-metal distances observed in other R2 structures, which show an even broader distance distribution centered around ~3.6 Å, and similar site heterogeneity has also been observed for related cofactors in other enzymes (see Refs. 29 and 30) and references therein). We consider these results as evidence that during diffraction data collection XPR altered the cofactor structures.

Metal and MnFe/FeFe Cofactor Contents—FeFe- and MnFe-containing *Ct*R2 samples were prepared, which contained air-oxidized (ox) or chemically reduced (red) proteins and are denoted *Ct*R2$_{FeFe}$^{ox}, *Ct*R2$_{FeFe}$^{red}, *Ct*R2$_{MnFe}$^{ox}, and *Ct*R2$_{MnFe}$^{red}. The sample conditions (29, 30) were chosen to allow for comparison of the cofactor properties in the native oxidized and reduced states with those of XPR-induced species.

Metal contents were in the range of about 0.5–0.7 mM manganese and 0.9–3.2 mM iron in the XAS samples, which contained about 1–2 mM R2 polypeptide (Table 1). The binding sites in *Ct*R2$_{FeFe}$ were occupied near quantitatively with close to two iron atoms per R2 polypeptide; manganese was at the

TABLE 1

Metal and protein concentrations and relative amounts of cofactor species

Metal concentrations were determined by TXRF. Relative amounts of cofactor species represent maximal figures, which were calculated on the basis of the metal and R2 polypeptide concentrations and assuming that all Mn ions were incorporated in MnFe sites. Values in parentheses were calculated under the assumption that all zinc ions were included in FeZn sites (114). Other transition metal species were negligible in the R2 samples.

Sample	R2	Mn	Fe	Zn	Mn/R2	Fe/R2	Zn/R2	MnFe	FeFe	FeZn
	mM	mM	mM	mM				%	%	%
CtR2$_{FeFe}^{red}$	0.8	0.04	1.37	0.44	0.05	1.71	0.55	6 (4)	94 (49)	0 (47)
CtR2$_{FeFe}^{ox}$	1.8	0.04	3.28	0.23	0.02	1.82	0.12	2 (1)	98 (92)	0 (7)
CtR2$_{MnFe}^{red}$	1.0	0.49	0.87	0.36	0.49	0.87	0.36	72 (57)	28 (1)	0 (42)
CtR2$_{MnFe}^{ox}$	1.3	0.72	1.32	0.21	0.55	1.02	0.16	71 (64)	29 (17)	0 (19)

detection limit. A slightly lower apparent occupancy was observed for CtR2$_{MnFe}$, in which the manganese content was ~55% of the iron content. The metal contents of oxidized and reduced samples were rather similar. These observations are in agreement with previous results (25, 29, 30, 71). An elevated Zn content was found only in the CtR2^{red} samples. The maximal relative amounts of MnFe and FeFe sites were calculated from the metal and R2 concentrations (Table 1), yielding close to 100% FeFe sites in CtR2$_{FeFe}$. In CtR2$_{MnFe}$, sufficiently high amounts (70%) of MnFe sites were obtained (Table 1), which allowed for determination of the properties of the hetero-metal sites by XAS.

Structure and XPR of the FeFe Cofactor—XANES spectra at the Fe K-edge were recorded for the CtR2$_{FeFe}$ samples (Fig. 2A). They revealed K-edge energies, which indicated close to 100% Fe(III) in CtR2$_{FeFe}^{ox}$, but about 70% Fe(III) and 30% Fe(II) in CtR2$_{FeFe}^{red}$. These values were obtained by comparison to iron reference compounds, revealing a K-edge energy difference of ~2.8 eV between the Fe(II) and Fe(III) levels (Table 2). Combining the XANES and TXRF data, ~100% Fe(III)Fe(III) sites for CtR2$_{FeFe}^{ox}$, but ~57% Fe(III)Fe(III) and ~43% Fe(III)Fe(II) for CtR2$_{FeFe}^{red}$ were calculated.

For monitoring of XPR of the initial Fe(III)Fe(III) cofactor, a series of consecutive. XAS scans were performed on single spots of CtR2$_{FeFe}^{ox}$ samples. Respective XANES spectra for about 2, 90, and 265 min of x-ray exposure at 20 K (Fig. 2A) revealed K-edge energies, which decreased from an initial mean oxidation state of 3 to a level of about 2.2, suggesting ~80% of Fe(II) after prolonged XPR (Table 2). A plot of the K-edge energies of all obtained XANES spectra *versus* the x-ray exposure periods revealed biphasic XPR kinetics at 20 K (Fig. 2B). A similar behavior was observed when the normalized x-ray fluorescence level at a constant excitation energy of 7123 eV in the iron K-edge was used as an alternative measure of XPR (Fig. 2B). Both data sets were well simulated using sums of two exponential functions with similar time constants (τ) of about 60 and 260 min and amplitudes close to 50% each (Fig. 2B, Table 3). We attribute these kinetic phases (i) to the more rapid formation of Fe(III)Fe(II) states, terminated after about 1.5 h, and (ii) to the slower reduction to the Fe(II)Fe(II) level, finished after about 7 h at 20 K. Kinetic XPR data for CtR2$_{FeFe}^{ox}$ at an increased temperature of 80 K still revealed biphasic behavior, but acceleration of both reduction phases compared with the 20 K data (Fig. 2B, inset); so that τ_1 and τ_2 were decreased to ~1 and ~18 min, respectively (Table 3).

Changes of the coordination geometries of the iron sites were assayed by analysis of the pre-edge features in the XANES (88) (Fig. 2A, inset). For CtR2$_{FeFe}^{ox}$, the small pre-edge amplitude
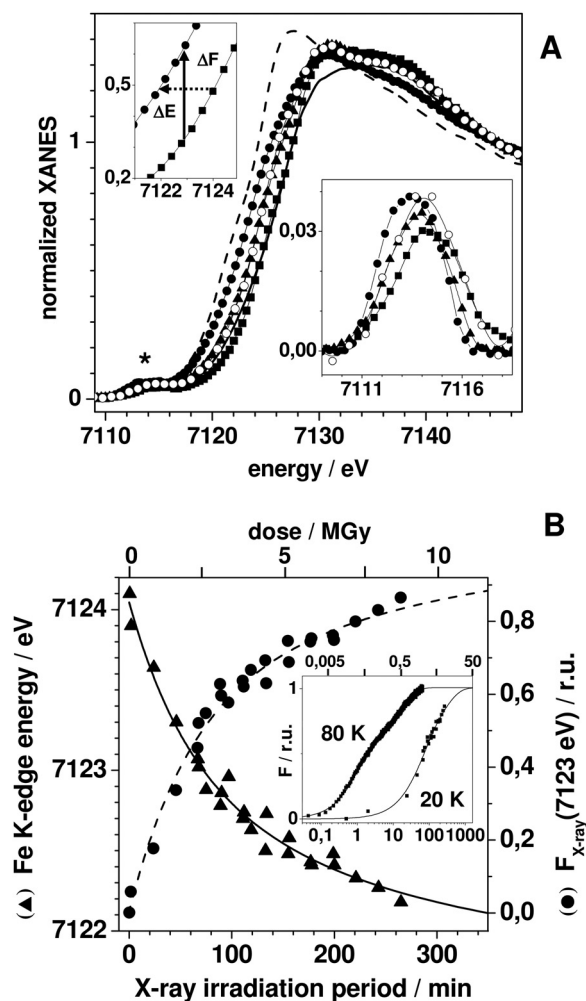

FIGURE 2. **XPR kinetics of the FeFe cofactor.** *A*, iron XANES spectra of CtR2$_{FeFe}^{ox}$ (*squares*) and CtR2$_{FeFe}^{red}$ (*open circles*) of CtR2$_{FeFe}$ samples initially in the oxidized (ox) state after x-ray exposure at 20 K for ~90 min (*triangles*) and ~260 min (*solid circles*), and of iron oxidation state references (Fe^{II}N$_4$O$_2$, *dashed line*; Fe^{III}N$_5$O, *solid line*; see Table 3). *Upper inset*, K-edge spectra around the 50% level of CtR2$_{FeFe}^{ox}$ and CtR2$_{FeFe}^{x260}$, the *arrows* mark the edge downshift (ΔE) and corresponding fluorescence intensity increase (ΔF) for an excitation energy of 7123 eV. *Lower inset*, expanded view of isolated pre-edge peaks in the XANES (*asterisk*). *B*, K-edge energies (*triangles*, *left y* axis) and x-ray fluorescence intensities at 7123 eV (*circles*, *right y* axis) at 20 K, together with the fit curves calculated using parameters in Table 3. *Inset*, time scan trace of the x-ray fluorescence intensity at 7123 eV at 80 K, K-edge data at 20 K, and fit curves (Table 3) on a logarithmic axis. Traces were normalized to unity amplitude after offset subtraction on the basis of the fit results. The given dose values (in *Gy*, gray = J kg^{-1}) are approximate and correspond to the incident dose, the absorbed dose in 1 mm of water for an energy of 7125 eV is ~77% of the incident dose. Dose values were calculated for an energy of 7125 eV = 1.14 × 10^{-14} joule, a flux (upper limit) of 10^{11} photons s^{-1}, and an irradiated volume of 0.2 mm^3 corresponding to 2.15 × 10^{-7} kg (aqueous buffer plus R2 protein contributing about 0.15 × 10^{-7} kg at 1.8 mM and a molecular mass of ~43 kDa).

TABLE 2

Manganese and iron K-edge energies and relative amounts of M(II) and (III) ions

K-edge energies reflect the 50% level of XANES spectra (Figs. 2 and 5), the error was ~0.15 eV. Oxidation state references are octahedral metal species, namely Mn(II) O_6 in hexaquo-Mn(II) in a 3 mM solution of $MnCl_2$, Mn(III)O_4N_2 in a powder sample of a synthetic Mn_2 complex (115), Fe(II)N_4O_2 in the non-heme iron site of bacterial photosynthetic reaction center protein (98), and Fe(III)N_5O in the heme of oxidized bovine hemoglobin in 15 mM solution. Indices xi specify the mean x-ray exposure in min. Metal (M) site amounts were calculated using linear relations between K-edge energies and oxidation states (Figs. 2B and 4; for $CtR2_{MnFe}^{ox}$ neglecting a minor Mn(IV) contribution). $CtR2_{MnFe}^{x-ray}$ denotes a state reached after ~130 min of XPR.

| sample	M	E_{K-edge}	ox. state	M(II),M(III) [%]
$Mn^{II}O_6$	Mn	6546.7	2.0	100,0
$Mn^{III}O_4N_2$		6549.5	3.0	0,100
$Fe^{II}N_4O_2$	Fe	7121.3	2.0	100,0
$Fe^{III}N_5O$		7124.1	3.0	0,100
$CtR2_{FeFe}^{red}$	Fe	7123.4	2.7	30,70
$CtR2_{FeFe}^{ox}$		7124.3	3.0	0,100
$CtR2_{FeFe}^{x1}$		7124.1	3.0	0,100
$CtR2_{FeFe}^{x90}$		7123.2	2.7	30,70
$CtR2_{FeFe}^{x260}$		7122.1	2.2	80,20
$CtR2_{MnFe}^{red}$	Mn	6547.9	2.4	55,45
	Fe	7122.8	2.6	45,55
$CtR2_{MnFe}^{ox}$	Mn	6550.0	3.2	0,100
	Fe	7124.0	3.0	0,100
$CtR2_{MnFe}^{x-ray}$	Mn	6548.1	2.5	50,50
	Fe	7121.7	2.3	70,30

TABLE 3

XPR kinetics for manganese and iron

Relative amplitudes (A) and time constants (τ) resulted from double-exponential simulations of K-edge energy (E) and X-ray fluorescence intensity (F) data for the two metals (Figs. 3B and 5), using appropriate offset values.

sample	M	T [K]	method	A1 [%]	τ1 [min]	A2 [%]	τ2 [min]
$CtR2_{FeFe}^{ox}$	Fe	20	E(K-edge)	54	57	46	253
			F(7123 eV)	56	58	44	266
		80	F(7123 eV)	54	1.0	46	18
$CtR2_{MnFe}^{ox}$	Mn	20	E(K-edge)	43	28	57	265
			F(6549 eV)	38	26	62	276
		80	F(6549 eV)	31	1.5	69	41
	Fe	20	E(K-edge)	44	81	56	348
			F(7123 eV)	39	75	61	360
		80	F(7123 eV)	26	1.1	74	40

suggested predominantly 6-coordinated Fe(III) ions, whereas the increased pre-edge peak at ~0.4 eV lower energy for $CtR2_{FeFe}^{red}$ suggested 5-coordinated iron at least in the 30% Fe(II) fraction. A pronounced increase and shift to lower energy of the pre-edge was observed for increasing x-ray exposure periods. Accordingly, this was explained by a change from 6-co-ordinated Fe(III) to 5-coordinated Fe(II) in the major sample fraction after prolonged XPR.

EXAFS on the native oxidized and reduced states, and on photoreduced $CtR2_{FeFe}$ samples was performed to study changes of interatomic distances at the metal cofactor (Fig. 3). The FTs of the EXAFS spectra (Fig. 3A, *inset*) of $CtR2_{FeFe}^{ox}$ and $CtR2_{FeFe}^{red}$ revealed relatively small differences, *e.g.* changes of the FT maxima reflecting Fe-Fe distances. Visual inspection of
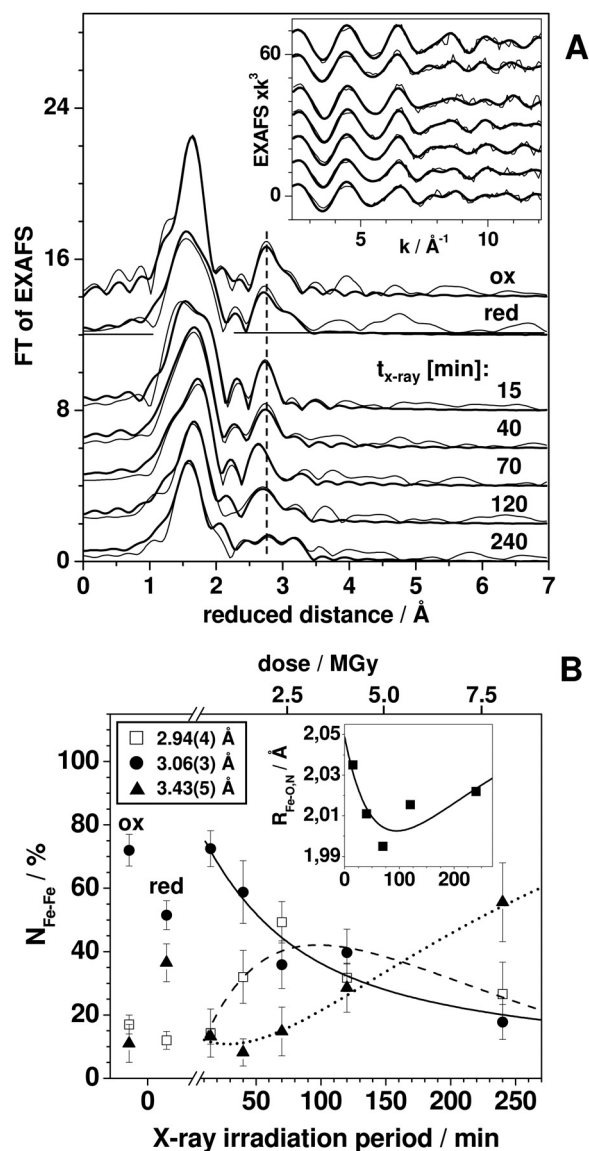
FIGURE 3. **EXAFS for XPR of the FeFe cofactor.** *A*, FTs (*thin lines*) of EXAFS spectra (*inset*) and simulation curves (*thick lines*) based on parameters in Table 4 (Fe-O,N distances); and *B* (Fe-Fe distances) for the indicated $CtR2_{FeFe}$ states and mean x-ray exposure periods. Spectra were vertically displaced for comparison. *B*, coordination numbers (N_{Fe-Fe}) for EXAFS data in *A* of 3 Fe-Fe distances for oxidized (*ox*) and reduced (*red*) $CtR2_{FeFe}$ samples (depicted at "0" levels, meaning for negligible XPR) and for $CtR2_{FeFe}^{ox}$ after the indicated mean XPR periods. Fe-Fe distance margins (in *parentheses*) and *vertical bars* denote the full range of R and N variations for different fit approaches (simulations of individual spectra or joint simulations of all spectra including variations in the fit restraints for Fe-O,N shells (40)). *Inset*, mean Fe-O,N distances calculated from the data in Table 4. Smooth curves show fits of the N values by sums of two exponential functions using time constants in Table 3 and appropriate offsets and amplitude signs. Given dose values are approximate and were calculated as detailed in the legend of Fig. 2.

the FTs for increasing x-ray exposure periods revealed systematic changes, for example, an initial shift to shorter distances and later diversification of the main FT maximum due to Fe-Fe distances and shifts of the main FT maximum due to Fe-ligand interactions (Fig. 3A).

By simulation of the EXAFS spectra (curve fitting) the structural changes were quantified (Fig. 3A). The main difference in $CtR2_{FeFe}^{red}$ in the first iron coordination sphere was an increase of the Fe-O,N bonds lengths and a slightly increased coordina-

TABLE 4

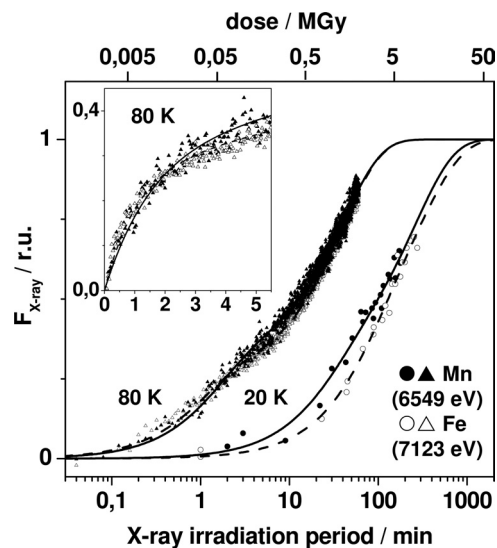**EXAFS simulation parameters for the first coordination shells of manganese and iron**

N, coordination number, R, interatomic distance; $2\sigma^2$, Debye-Waller factor, R_F, fit error sum (75) calculated for reduced distances of FTs in the range of 1.0–3.5 Å. (*) Values that were kept constant in the fit procedures, (#) respective $2\sigma^2$ values were coupled to yield the same values for both coordination shells. For respective fit curves to the EXAFS spectra see Figs. 3A and 6.

	N [per Fe] / R [Å] / $2\sigma^2$ x10^3 [Å^2]		R_F [%]
Fe	**Fe-O**	**Fe-O,N**	
CtR2$_{FeFe}$^{red}	4.75 / 1.98 / 20	1.25 / 2.16 / 2*	16.7
CtR2$_{FeFe}$^{ox}	3.95 / 1.96 / 11	2.05 / 2.11 / 2*	17.1
CtR2$_{FeFe}$^{x15}	3.32 / 1.95 / 10	2.68 / 2.14 / 2*	20.3
CtR2$_{FeFe}$^{x40}	3.55 / 1.95 / 12	2.45 / 2.10 / 2*	14.9
CtR2$_{FeFe}$^{x70}	4.55 / 1.97 / 27	1.44 / 2.09 / 2*	17.5
CtR2$_{FeFe}$^{x120}	4.87 / 2.01 / 38	1.13 / 2.05 / 2*	22.8
CtR2$_{FeFe}$^{x240}	5.09 / 2.03 / 36	0.91 / 1.98 / 2*	25.0
Mn	**Mn-O**	**Mn-O,N**	
CtR2$_{MnFe}$^{ox}	1.93 / 1.69 / 24$^{\#}$	4.07 / 1.95 / 24$^{\#}$	19.8
CtR2$_{MnFe}$^{red}	1.16 / 1.74 / 26$^{\#}$	4.84 / 2.09 / 26$^{\#}$	14.5
CtR2$_{MnFe}$$^{x-ray}$	1.54 / 1.85 / 15$^{\#}$	4.45 / 2.15 / 15$^{\#}$	17.7
Fe	**Fe-O**	**Fe-O,N**	
CtR2$_{MnFe}$^{ox}	1.08 / 1.88 / 18$^{\#}$	4.92 / 2.02 / 18$^{\#}$	25.6
CtR2$_{MnFe}$^{red}	4.56 / 2.01 / 12$^{\#}$	1.44 / 2.44 / 12$^{\#}$	20.4
CtR2$_{MnFe}$$^{x-ray}$	0.90 / 1.79 / 21$^{\#}$	5.20 / 2.04/ 21$^{\#}$	29.3

FIGURE 4. **XPR kinetics of the MnFe cofactor.** Data represent fluorescence intensity levels at energies in the manganese or iron K-edges, derived from XANES spectra (at 20 K, see Fig. 5) or time scan traces (80 K) and are shown on a logarithmic time axis. *Lines* (*solid*, Mn; *dashed*, Fe) represent double-exponential fits with time constants in Table 3. *Inset*, data at 80 K on a linear time axis. The incident dose values are approximate (the absorbed dose in 1 mm of water for 6550 eV is ~85% of the incident dose); dose values were calculated using an energy of 6550 eV = 1.05×10^{-14} joule, an irradiated volume of 2.11×10^{-7} kg (buffer plus about 0.11×10^{-7} kg of R2 protein at 1.3 mM, and further parameters given in the legend of Fig. 2.

tion number (N) but largely increased Debye-Waller parameter ($2\sigma^2$) for the shorter bonds, compared with CtR2$_{FeFe}$^{ox} (Table 4). In particular the $2\sigma^2$ increase suggested significant amounts of 5-coordinated iron ions in CtR2$_{FeFe}$^{red}. Fe-Fe distances (R) of about 2.95, 3.05, and 3.40 Å readily accounted for the Fe-Fe interactions. The 3.05-Å distance represented the main species in CtR2$_{FeFe}$^{ox} (~70%), whereas for CtR2$_{FeFe}$^{red} it was the ~3.40 Å distance (~55%) (Fig. 3B). The ~2.95-Å distance (~10%) was at the detection limit. The Fe-Fe distance changes and coordination numbers in oxidized and reduced samples suggested that in the Fe(III)Fe(III) site the iron atoms are separated by ~3.05 Å and ~3.40 Å distance accounts for an Fe(III)Fe(II) site (29, 30).

Simulations of a series of EXAFS spectra for the x-ray-exposed CtR2$_{FeFe}$ samples revealed the following (Fig. 3B, Table 4). The structural parameters for ~15 min XPR were similar to those for CtR2$_{FeFe}$^{ox}, revealing a predominant contribution of the ~3.05 Å Fe-Fe distance. For increasing x-ray exposure periods up to ~240 min, for the main Fe-O shell a simultaneous increase of the coordination number (N), the Debye-Waller parameter ($2\sigma^2$), and the bond-length (R) were determined, whereas for the initially longer second Fe-O,N interaction decreased N and R values (for constant $2\sigma^2$) were obtained (Table 4). The mean Fe-ligand bond lengths, however, revealed an initial decrease up to ~100 min XPR and an increase for longer periods (Fig. 3B, *inset*). Also for CtR2$_{FeFe}$^{red}, increased N and $2\sigma^2$ values for the Fe-O shell compared with CtR2$_{FeFe}$^{ox} were observed. These effects were explained by accumulation of the 5-coordinated Fe(II) during XPR.

For the Fe-Fe distances (Fig. 3B), an initial increase of the relative coordination number of the ~2.95 Å distance to ~50% after ~70 min of x-ray exposure occurred at the expense of the

~3.05 Å distance. It was followed by a decrease of the ~2.95-Å contribution and a concomitant increase of a distance close to ~3.45 Å to ~55% after 240 min. The kinetic behavior of the three Fe-Fe distances was reasonably well described using the same time constants as determined for XPR from the XANES analysis (Fig. 3B). This suggested an Fe-Fe distance shortening from ~3.05 Å to ~2.95 Å for the initial Fe(III)Fe(III) → Fe(III)-Fe(II) reduction step, which was followed by an elongation from ~2.95 Å to ~3.45 Å upon the Fe(III)Fe(II) → Fe(II)Fe(II) transition.

Structure and XPR of the MnFe Cofactor—The XPR kinetics of CtR2$_{MnFe}$^{ox} samples were monitored using similar approaches as described above (Fig. 4). Biphasic reduction behavior was observed both at the manganese and iron K-edges. Kinetic simulations of the 20 K data showed that the first phase was by a factor of about 5–10 faster than the second phase for manganese and iron (Table 3). The time constants of the two phases for manganese reduction were by factors of about 1.5–2.5 smaller than the ones for iron reduction. At 80 K, pronounced acceleration of reduction resulted in quite similar kinetics for both metal species (Table 3). Overall, the time constants for reduction of manganese and iron for CtR2$_{MnFe}$ and CtR2$_{FeFe}$ samples, initially containing mostly Mn(III) and Fe(III), were similar within a factor of ~2 at both 20 and 80 K.

We note that a minor Mn(IV) contribution in CtR2$_{MnFe}$^{ox} was suggested by the XANES spectrum (see below). However, the initial reduction phase of Mn(IV)Fe(III) sites has been found to be ~150 faster than the next step (30). This suggested τ values of about 0.3 and 0.01 min for Mn(IV)Fe(III) reduction at 20 and 80 K under the present conditions, which was at the kinetic resolution limit. Small amplitudes due to Mn(IV)Fe(III) reduction accordingly were not discernable for CtR2$_{MnFe}$.
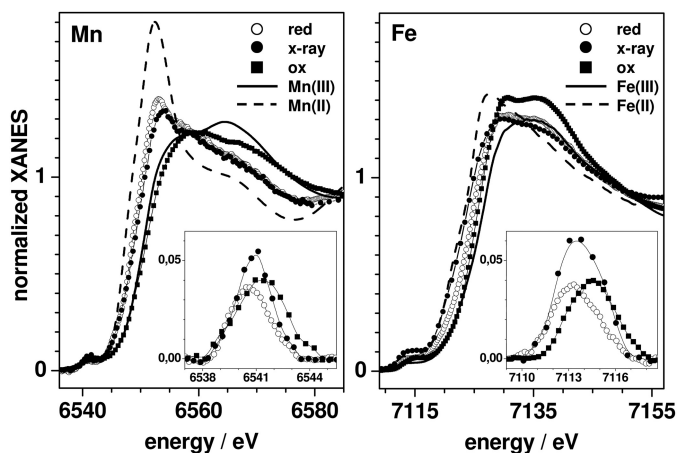
FIGURE 5. **Reduction of the MnFe cofactor monitored in the XANES.** *Left*, manganese K-edge spectra, and *right*, iron K-edge spectra of CtR2$_{MnFe}$ in the oxidized (*ox*) and reduced (*red*) states and after a mean x-ray exposure of CtR2$_{MnFe}$^{ox} of ~130 min (x-ray), together with spectra of respective oxidation state references (Table 2). *Insets*, corresponding isolated pre-edge features in magnification.

XANES spectra at the manganese and iron K-edges for CtR2$_{MnFe}$^{ox}, CtR2$_{MnFe}$^{red}, and for a state obtained after prolonged XPR denoted CtR2$_{MnFe}$$^{x-ray}$ are shown in Fig. 5. The spectrum of CtR2$_{MnFe}$$^{x-ray}$ resulted from summation of spectra for about 30–210 min x-ray exposure (mean of ~130 min) and thus represents the average over several manganese and iron oxidation states. Compared with manganese reference compounds, the manganese and iron edge energies of CtR2$_{MnFe}$^{ox} were close to the trivalent level; a minor Mn(IV) contribution (~20%) was implied by the somewhat higher manganese edge energy (Table 2). For CtR2$_{MnFe}$^{red}, the edge energies suggested about ~50% of each Mn/Fe(III) and Mn/Fe(II), neglecting the Mn(IV) contribution. CtR2$_{MnFe}$$^{x-ray}$ accordingly contained Mn/Fe(III) and Mn/Fe(II) in about 50/30% and 50/70% proportions.

Metal site geometry changes again were deduced from the pre-edge features (Fig. 5, *insets*). Small pre-edge amplitudes for CtR2$_{MnFe}$^{ox} suggested predominantly 6-coordinated (*i.e.* near-octahedral) Mn(III) and Fe(III) ions. The diminished manganese and iron pre-edge peaks at >1 eV lower energies for CtR2$_{MnFe}$^{red} implied a further symmetrization of the coordination of the divalent metal ions. At variance with the latter behavior, CtR2$_{MnFe}$$^{x-ray}$ showed increased manganese and iron pre-edge features at lower energies compared with CtR2$_{MnFe}$^{ox}. This suggested formation of 5-coordinated manganese and iron ions after prolonged XPR.

Visual inspection of the EXAFS spectra of the three CtR2$_{MnFe}$ states (Fig. 6) revealed that the main FT maximum of the manganese EXAFS due to first-sphere Mn-O,N distances was at higher distances in CtR2$_{MnFe}$^{red} and CtR2$_{MnFe}$$^{x-ray}$ compared with CtR2$_{MnFe}$^{ox}, suggesting an overall increase of the bond lengths for Mn(II). Less pronounced changes of the main FT maximum due to Fe-O,N bonds were observed. In the manganese EXAFS, two FT maxima at reduced distances of 2–3 Å were attributed to Mn-Fe interactions. For CtR2$_{MnFe}$^{ox} the first maximum was larger than the second one, whereas for CtR2$_{MnFe}$^{red} this was reversed. For CtR2$_{MnFe}$$^{x-ray}$ the main Mn-Fe FT peak was even at larger distances than for the other
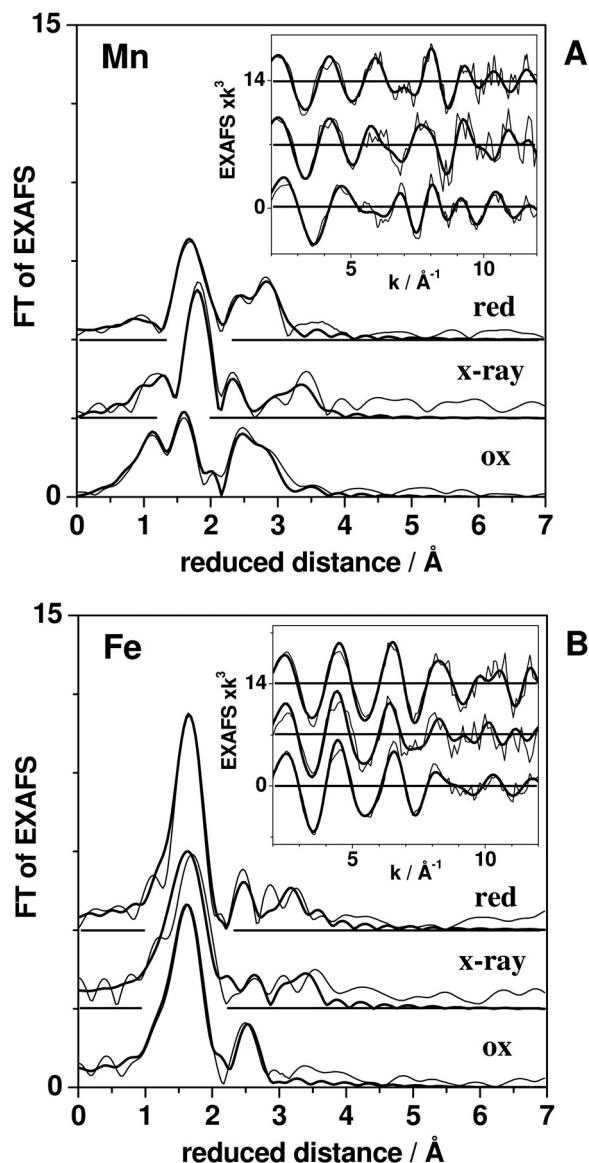

FIGURE 6. **EXAFS of the MnFe cofactor.** FTs (*thin lines*) of manganese (*A*) and iron (*B*) EXAFS spectra (*insets*) of CtR2$_{MnFe}$^{ox}, CtR2$_{MnFe}$^{ox}, and CtR2$_{MnFe}$$^{x-ray}$, together with simulation curves (*thick lines*) based on the parameters indicated in Table 4 (Mn/Fe-O,N distances) and Fig. 7 (metal-metal distances).

two samples. The iron EXAFS of CtR2$_{MnFe}$^{ox} showed one main Fe-Mn,Fe distance, whereas for CtR2$_{MnFe}$^{red} and CtR2$_{MnFe}$$^{x-ray}$, several Fe-Mn,Fe distances were resolved (Fig. 6).

The simulation results for the manganese and iron EXAFS spectra are summarized in Table 4 (first coordination sphere) and Fig. 7 (metal-metal distances). In CtR2$_{MnFe}$^{ox}, Mn-O,N distances of ~1.70 Å likely were attributable to bonds between manganese and metal-bridging μO species; the ~1.95 Å distances reflected μO(H) bridges and terminal Mn-O,N bonds (30). The Mn-O,N bond lengths for CtR2$_{MnFe}$^{red} and CtR2$_{MnFe}$$^{x-ray}$ were increased, accompanied by moderate coordination number changes. The iron EXAFS indicated that the Fe-O,N bonds overall were ~0.2 Å longer than the Mn-O,N bonds (Table 4). For CtR2$_{MnFe}$^{ox} the two Fe-O,N bond lengths differed by ~0.14 Å. In CtR2$_{MnFe}$^{red} the shorter Fe-O,N bonds were elongated compared with CtR2$_{MnFe}$^{ox} to even ~2.4 Å,
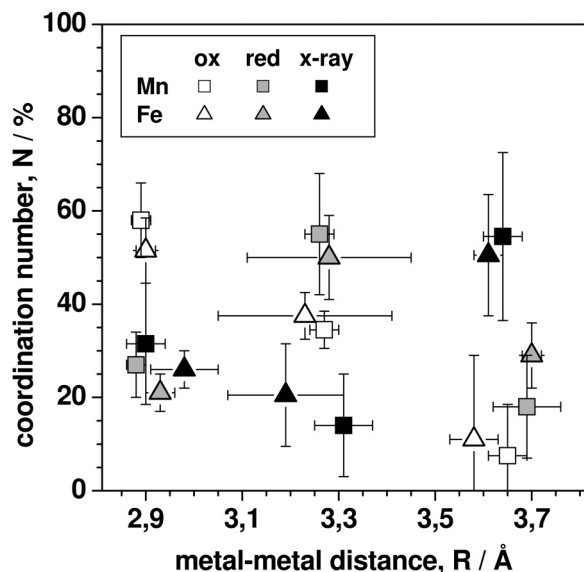
VOLUME 288·NUMBER 14·APRIL 5, 2013

FIGURE 7. **Metal-metal coordination numbers and distances for MnFe sites.** Data correspond to simulations of EXAFS data for three CtR2$_{MnFe}$ states in Fig. 6. *Vertical* and *horizontal bars* denote the full variation range of N and R values as obtained for different fit approaches (individual or joint EXAFS simulations and variations in the fit restraints for the Mn/Fe-O,N shells; see text).

possibly suggesting elongation of Fe-N$_{His}$ bonds. The first-sphere iron coordination of CtR2$_{MnFe}$$^{x-ray}$ was more similar to CtR2$_{MnFe}$^{ox}, suggesting relatively minor changes of the Fe-O,N bonds.

At least three metal-metal distances were discernable both in the manganese and iron EXAFS spectra (Fig. 7). The main Mn-Fe distance in CtR2$_{MnFe}$^{ox} was ~2.90 Å (~55%) and minor contributions of a ~3.30-Å distance (~35%) were observed. CtR2$_{MnFe}$^{red} showed opposite magnitudes (~25%, ~50%) of contributions from these two distances. Similar metal-metal distances in CtR2$_{MnFe}$ have previously been attributed to Mn(IV)/(III)Fe(III) (~2.90 Å) and Mn(II)Fe(III) (~3.3 Å) sites (29, 30, 66). Here, the ~2.90 Å distance mostly reflected the Mn(III)Fe(III) cofactor, because Mn(IV) contributions were small. We note that in the iron EXAFS the ~3.3 Å distance was less well defined than in the manganese EXAFS so that several equivalent fits with distances around 3.1–3.4 Å were possible. This reflects contributions from the minor amounts of FeFe species (compare Table 1 and Fig. 3B).

In CtR2$_{MnFe}$$^{x-ray}$, the main metal-metal distance was ~3.65 Å (~55%) and contributions from the other two distances apparently were small (Fig. 7). A ~3.65 Å distance was close to the detection limit in CtR2$_{MnFe}$^{ox} and CtR2$_{MnFe}$^{red}. Accordingly, we assign the ~3.65 Å distance to the main XPR-induced state of the MnFe site in CtR2$_{MnFe}$$^{x-ray}$. Comparison of the TXRF, XANES, and EXAFS results revealed that the ~3.65 Å distance most likely reflects a Mn(II)Fe(II) state of the cofactor, as preferably produced by XPR at cryogenic temperatures. That the ~2.9 Å distance in CtR2$_{MnFe}$$^{x-ray}$ remained at a level, which was comparable with CtR2$_{MnFe}$^{red}, may be explained by a similar initial metal-metal distance shortening as observed for CtR2$_{FeFe}$.

Model Structures for XPR from DFT—Density functional theory calculations were employed to generate model structures
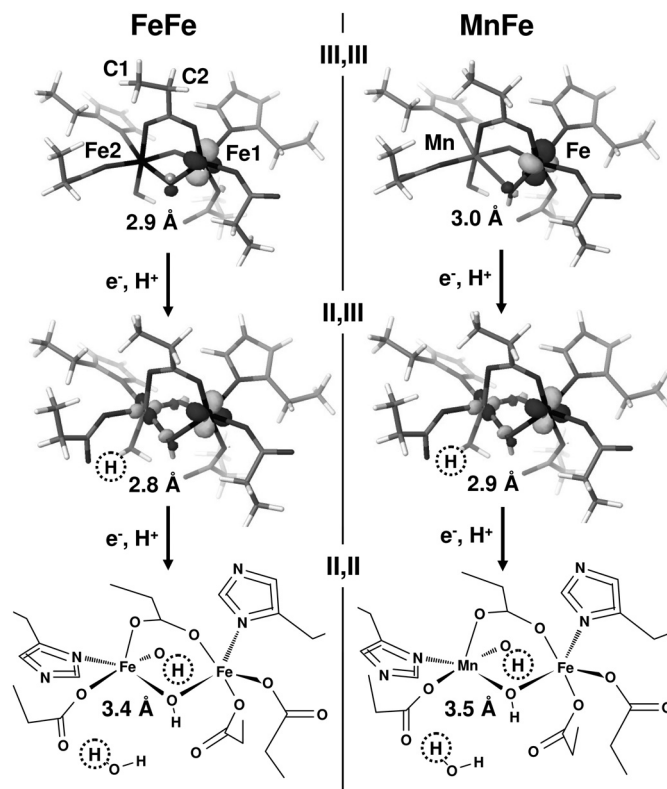

FIGURE 8. **DFT structures for oxidized and single or double reduced FeFe and MnFe sites.** The (III,III) states (*top*) were calculated on the basis of the PDB 1SYY structure of wild type CtR2$_{FeFe}$ (replacing Fe2 by Mn, *right*). *Middle* and *bottom* structures were calculated after additions of 1/2 electron(s) and 1/2 proton(s) (*dotted circles*); Fe2/Mn-OH$_2$ and Fe1/Fe-OH distances in the (II,II) states are >3 Å. (III,III) and (III,II) structures show the localizations of the lowest energy unoccupied molecular orbitals (*LUMO*) with β spin orientation. The α-spin LUMOs were largely located at Fe2 for the FeFe sites and at manganese for the MnFe sites (not shown). The (II,II) structures in stick representation (most protons omitted for clarity) exemplify the positions of hetero-atoms in all structures. Atoms denoted *C1* and *C2* for Glu-120 were fixed at their crystallographic positions for all amino acid ligands in the DFT calculations. Approximate metal-metal distances are indicated, for further parameters, see supplemental Table S1.

for the native and XPR-modified cofactors. The restricted mobility of amino acids during XPR at cryogenic temperatures was simulated by fixation of carbon atoms during geometry optimization after addition of 1 electron to the initial Fe(III)-Fe(III) and Mn(III)Fe(III) sites or 2 electrons to the singly reduced structures. Structures were calculated for additions of electrons only or for balancing of respective surplus negative charges by protons.

Comparison of more than 20 DFT-optimized structures revealed the following (supplemental Table S1, Fig. 8). When only one C-atom of the side chains (C1 in Fig. 8) was fixed during geometry optimizations of single and double reduced states and no protons were added, the resulting structures showed excessive changes, for example, breaking the Glu-120 carboxylate and μO(H) bridges, detachment of histidine ligands, and pronounced Glu ligand reorientations, leading, *e.g.* to 4-coordinated manganese and iron ions. We consider such large scale geometry changes as unlikely at cryogenic temperatures. Fixation of two C-atoms resulted in less severe structural changes, but the tendency for carboxylate bridge breaking and histidine detachment remained, still causing mostly low coor-

dination numbers as well as metal-metal distance elongation already for single-electron reduction in some cases. The structural changes after additions of electrons and protons depended on the actual protonation site. As a trend, less pronounced changes were observed so that higher metal coordination numbers prevailed (supplemental Table S1).

Best agreement with the structural parameters from XAS was achieved by proton addition first to terminal OH groups at Fe2 or manganese in the single reduced sites and second to μO(H) bridges in the double reduced sites, both for the FeFe and MnFe structures (Fig. 8). In this case, the first reduction for both structures resulted in a shortening of the metal-metal distance by ~0.1 Å in the mixed-valent states, similar to the experiment. This was followed by elongations to >3 Å of Fe-μO(H) and Fe/Mn-OH$_2$ bonds, resulting in 5-coordinated Fe(II) and Mn(II) ions after the second reduction step and in a pronounced elongation of the metal-metal distance to about 3.4–3.5 Å, as also inferred from the experimental data (Fig. 8). For a brief account on the electronic configurations of the DFT structures and their possible relationship to the redox potentials see supplemental Table S1.

DISCUSSION

Structures of FeFe and MnFe Cofactors—Our results suggest the following native structures of FeFe and MnFe cofactors in *Ct*R2. For the trivalent sites (L = Glu/Asp and His ligands), L$_3$(HO)Fe(III)(μO)(μOH)Fe(III)L$_4$ (Fe-Fe ~3.05 Å) and L$_3$(HO)Mn(III)(μO)(μOH)Fe(III)L$_4$ (Mn-Fe ~2.90 Å) core configurations are proposed (Fig. 9). This is in agreement with previous assignments (29, 30, 44). Chemical reduction of the (III,III) states by one electron at room temperature likely induces breaking of a μO(H) bridge, presumably accompanied by a protonation, which explains the ~0.4 Å metal-metal distance increase (4, 43, 63, 75, 89) and metal-ligand bond elongations in the (III,II) cofactors. Fe(III) reduction leads to 5-coordinated Fe(II), at least in the FeFe site, whereas in particular for the MnFe site, Mn/Fe(II) formation may lead to the (partial) loss of one ion and to a remaining 6-coordinated site. For the (II,II) sites, the absence of μO(H) metal bridges is likely, resulting in metal-metal distances exceeding 3.7 Å (Fig. 9), similar to the distances observed in crystal structures of reduced R2 proteins (29, 30).

The structural differences between the FeFe and MnFe sites in *Ct*R2 presumably are relatively subtle. On the structural basis, the reasons for the preferential use of differently metallated sites in the class-Ia RNRs (FeFe), in the class-Ib RNRs (MnMn), and in the tyrosine-radical lacking R2 protein of class-Ic *Ct* RNR (MnFe) therefore remain elusive. Tuning of the redox potential, for example, by different protonation states of bridging oxides (29, 30, 44, 90, 91), thus may play an important role in the functional diversification of the dimetal-oxygen cofactors.

Structural Changes during XPR—The main structural changes at the FeFe and MnFe cofactors of *Ct*R2 that are induced by XPR at cryogenic temperatures apparently differ from the changes occurring during chemical reduction at room temperature (Fig. 9). At low temperatures, single electron reduction of the (III,III) cofactors causes even a ~0.1 Å short-
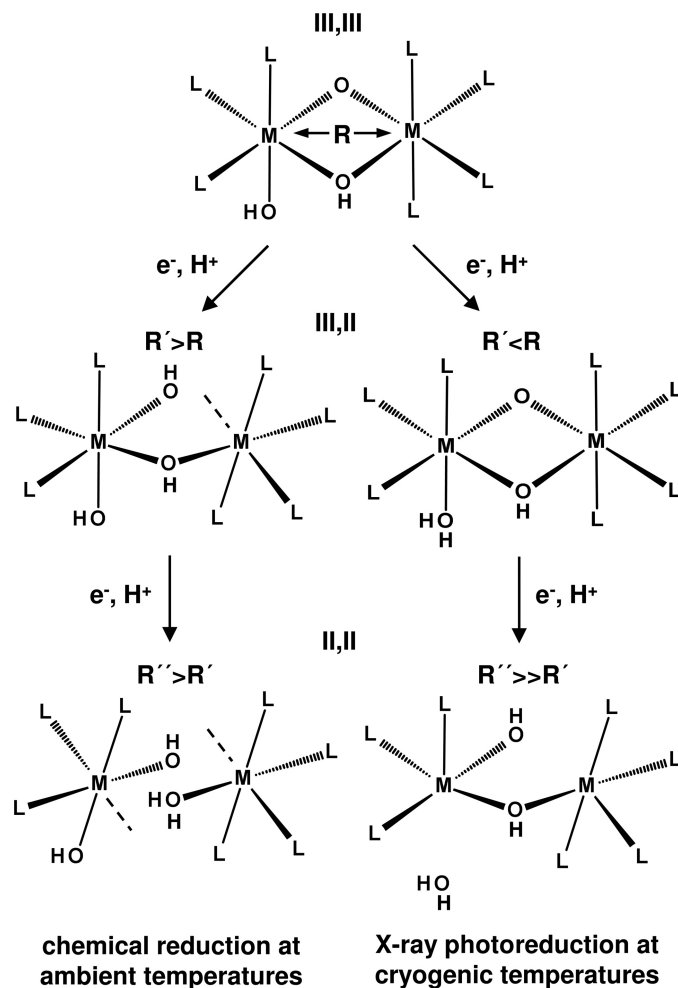

FIGURE 9. Proposed structural and redox changes at FeFe and MnFe cofactors for chemical reduction at ambient temperatures and XPR at cryogenic temperatures. Assignments represent a combination of our XAS and DFT results (M = metal, L = ligands). Approximate metal-metal distances (average of FeFe and MnFe sites): R(III,III), ~3.0 Å; R' (III,II), ~3.4 Å (ambient temperatures) and ~2.9 Å (XPR); R''(II,II), ≥3.7 Å (ambient temperatures) and ~3.5 Å (XPR). *Dashed lines* denote a sixth ligand (*e.g.* a water molecule), which possibly is bound upon reduction at ambient temperatures (for example, when one metal ion is lost in the (II,II) states). Positions and numbers of protonation sites and O(H$_{1,2}$) groups are tentative, but in plausible agreement with the features of the (III,III) states and the structural changes upon reduction.

ening of the metal-metal distance and only relatively minor bond length changes in the first-sphere metal coordination, but leaves the μO(H) bridging intact. A possible explanation for this behavior is the associated protonation, for example, of a terminal OH group. Reduction of the (III,II) states induces more severe changes, such as formation of 5-coordinated Fe/Mn(II) ions, which likely is explained by the breaking of at least one μO(H) bridge and/or of a terminal metal-OH$_2$ bond. This leads to a ≥0.5 Å elongation of the metal-metal distances in the (II,II) states (Fig. 9). Apart from minor differences in the overall site geometries, this sequence of events seems to hold for FeFe and MnFe cofactors.

The structural changes during XPR at 20 K have to involve movements of metal ions and (first-sphere) ligand atoms on the order of 1 Å or less, to explain the observed bond length changes. Changes of similar magnitude have been inferred from

XPR studies of other metalloproteins and synthetic complexes (53, 54, 58, 60, 61, 92–94). XPR even has been suggested as a tool for studying reduced states of metal cofactors (52, 53, 56, 57). In the case of *Ct*R2, our data suggest that both the mixed valence and fully reduced states of the FeFe and MnFe cofactors differ from their counterparts formed at ambient conditions. Presumably, this reflects the limited mobility of amino acid groups and water species in the frozen state. The XPR-induced states of dimetal-oxygen cofactors thus may have limited physiological relevance.

Our DFT results suggest that protonation events may play a role in the compensation of XPR-induced metal-centered charges even at 20 K. Indeed, proton movements in proteins and model systems can occur at low temperatures at least within a single hydrogen bond, if not over longer distances within extended hydrogen-bonded networks (95–97). This may be taken as evidence that terminal and/or metal-bridging O(H) ligands in *Ct*R2 are integrated in hydrogen-bonding interactions, for example, with water molecules. Water molecules in hydrogen-bonding distance, for instance, to metal-binding carboxylates, indeed were found in high-resolution R2 structures (39, 99, 100). The proton distribution in XPR-induced structures thus may significantly differ from the respective native oxidation states.

XPR Kinetics and Redox Potentials—Metal site reduction during XPR mostly is anticipated to result from electron transfer from radical sites, which have captured photoelectrons produced after core level excitations mainly of C-, O-, and N-atoms of the protein matrix (46). In addition, the XPR rates for the R2 cofactors may be expected to be proportional to their redox midpoint potentials (E_m) (30, 60, 101).

The XPR rates for the Fe(III)Fe(III) and Mn(III)Fe(III) cofactors differ by less than a factor of 2 (30), pointing to E_m values for the FeFe and MnFe cofactors, which are similar within about 150 mV (74, 102–103). The absolute E_m values for the Mn(IV)Fe(III) states presumably are on the order of 1 V (30) and the slower XPR of the (III,III) states thus suggests a significant E_m drop (104). A similar E_m implies relatively minor structural differences between the FeFe and MnFe sites at least in the (III,III) states, as observed.

Biphasic XPR kinetics were found for both the FeFe and MnFe sites. For the Fe(III)Fe(III) cofactor, this is straightforwardly explained by sequential Fe(III)Fe(II) and Fe(II)Fe(II) formation. For the MnFe cofactor, similar XPR rates for Mn(III) and Fe(III), in particular at 80 K, imply reduction of either ion at about equal probability. At first glance, the Mn(III) and Fe(III) ions thus seem to possess a similar E_m. However, our DFT results suggested reduction first of the iron ion (supplemental Table S1). The even faster manganese reduction at 20 K therefore may be explained by the ~1.5-times larger absorption of the protein at the lower manganese K-edge energies, *i.e.* creation of more reducing sites within a given XPR period. This could lead to the apparent inversion of manganese and iron reduction rates.

Implications for X-ray Crystallography of Dimetal-Oxygen Cofactors—Our present and previous data (29, 30, 66) indicate that XPR of high-valent FeFe and MnFe sites in *Ct*R2 and also in the standard type R2 protein from mouse can occur within sec-

onds to minutes already under XAS conditions. The respective doses (at 80 K) are at least 100 times smaller than those resulting in radiation damage of amino acid groups (46, 105).

Using an x-ray flux of $\sim 10^{11}$ photons s^{-1} at the iron and manganese K-edges as the upper limit and a spot size on the sample of ~ 0.2 mm^2, time constants of about 1–1.5 min (mean of ~70 s) for the (III,III) states and 20–40 min (mean of ~2000 s) for the (III,II) states were observed at 80 K, which is close to the 100 K often used in crystallography. A linear dose-rate relationship for the R2 cofactor reduction is suggested by the ~10-fold decrease of the time constant from ~3500 to ~350 s (at 20 K) of (III,III) reduction for a flux increase from $\sim 10^{11}$ photons s^{-1} used here to $\sim 10^{12}$ photons s^{-1} used previously (30). A typically more focused beam of 50 μm diameter for crystallography, *i.e.* a spot size of 0.002 mm^2, and a similar flux of $\sim 10^{11}$ photons s^{-1} therefore are expected to cause about 100 times faster XPR, *i.e.* time constants of 0.7 s for the (III,III) states and 20 s for the (III,II) states. A flux of $\sim 10^{13}$ photons s^{-1} (or more) of undulator crystallography beamlines thus decreases both time constants to far below 1 s. That these estimates are realistic is exemplified by the observed reduction of the Mn(IV)Fe(III) site in *Ct*R2 at 20 K within ~2 s at $\sim 10^{12}$ photons s^{-1} (30).

These results imply that for typical x-ray crystallography conditions, XPR of dimetal-oxygen cofactors is unavoidable. Moreover, this will not improve much for the use of liquid-helium temperatures, radical quenching agents (106), acquisition of only a few frames per crystal spot, moderately diminished doses, and faster detector readout. Accordingly, the initial high-valent sites in the crystals were mostly reduced to the (II,II) level. The respective metal-metal distance spread thus may in part reflect the remnants of (III,II) states. Further evidence for this view comes from our result that the Fe/Mn-Fe distances of 3.4–3.7 Å of the XPR-induced (II,II) states match the distances in most R2 structures, irrespective of the initial valence state (29, 30). Notably, the XAS-derived metal-metal distances for the (III,III) states of ~3 Å are considerably shorter than most of the crystallographic distances even for an upper-limit coordinate error of ~0.4 Å. The broad distribution of metal coordination motifs in the crystals may thus be due to the superimposition of several XPR-induced conformations.

Crystallographic information for initial (II,II) sites, which will not become further reduced, should be more reliable. However, in these states the metal complex is labilized, leading to single-metal sites and/or to heterogeneity in amino acid and oxygen species ligation geometries. The question arises why the significant XPR-induced structural changes at the metal site still allow for high-resolution crystallographic coordinates. The likely reason for this is that XPR is terminated already during the first few seconds of diffraction data collection and thereafter, the low-valence configuration of metal ions and ligands is stable.

In conclusion, crystal structures of higher valence states exceeding (II,II) or perhaps (III,II) levels of highly oxidizing dimetal-oxygen cofactors cannot be reliably obtained by conventional crystallography. A similar situation has been encountered for other types of high-potential metal cofactors (70, 107). The recent inauguration of fourth generation synchrotron radiation sources based on free electron-laser techniques seems to

offer a way to overcome the XPR problem (108–110). Using femtosecond x-ray pulses, XPR may be outrun by termination of the scattering process prior to initiation of the photoelectron cascade. The first structures for the free electron-laser approach using protein nanocrystals at room temperature have been reported even for radiation-sensitive systems, albeit at moderate resolution (111, 112). However, there is no principal limitation toward high resolution structures (113). Femtosecond crystallography on the superfamily of enzymes containing dimetal-oxygen cofactors appears to be an excellent scientific case for this emerging technique to obtain structures of high-valent intermediates.

REFERENCES

1. Cotruvo, J. A., and Stubbe, J. (2011) Class I ribonucleotide reductases. Metallocofactor assembly and repair *in vitro* and *in vivo*. *Annu. Rev. Biochem.* **80,** 733–767

2. Nordlund, P., and Reichard, P. (2006) Ribonucleotide reductases. *Annu. Rev. Biochem.* **75,** 681–706

3. Sjöberg, B. M., and Gräslund, A. (1983) Ribonucleotide reductase. *Adv. Inorg. Biochem.* **5,** 87–110

4. Tinberg, C. E., and Lippard, S. J. (2011) Dioxygen activation in soluble methane monooxygenase. *Acc. Chem. Res.* **44,** 280–288

5. Westerheide, L., Pascaly, M., and Krebs, B. (2000) Methane monooxygenase and its related biomimetic models. *Curr. Opin. Chem. Biol.* **4,** 235–241

6. Lange, S. J., and Que, L., Jr. (1998) Oxygen activating nonheme iron enzymes. *Curr. Opin. Chem. Biol.* **2,** 159–172

7. Högbom, M. (2010) The manganese/iron-carboxylate proteins. What is what, where are they, and what can the sequences tell us? *J. Biol. Inorg. Chem.* **15,** 339–349

8. Krebs, C., Matthews, M. L., Jiang, W., and Bollinger, J. M., Jr. (2007) AurF from *Streptomyces thioluteus* and a possible new family of manganese/iron oxygenases. *Biochemistry* **46,** 10413–10418

9. Herrick, J., and Sclavi, B. (2007) Ribonucleotide reductase and the regulation of DNA replication. An old story and an ancient heritage. *Mol. Microbiol.* **63,** 22–34

10. Brignole, E. J., Ando, N., Zimanyi, C. M., and Drennan, C. L. (2012) The prototypic class Ia ribonucleotide reductase from *Escherichia coli*. Still surprising after all these years. *Biochem. Soc. Trans.* **40,** 523–530

11. Kolberg, M., Strand, K. R., Graff, P., and Andersson, K. K. (2004) Structure, function, and mechanism of ribonucleotide reductases. *Biochim. Biophys. Acta* **1699,** 1–34

12. Bollinger, J. M., Jr., and Krebs, C. (2006) Stalking intermediates in oxygen activation by iron enzymes. Motivation and method. *J. Inorg. Biochem.* **100,** 586–605

13. Que, L., Jr. (1991) Oxygen activation at the diiron center of ribonucleotide reductase. *Science* **253,** 273–274

14. Que, L., Jr. (2004) The oxo/peroxo debate. A nonheme iron perspective. *J. Biol. Inorg. Chem.* **9,** 684–690

15. Han, W. G., Liu, T., Lovell, T., and Noodleman, L. (2006) Seven clues to the origin and structure of class-I ribonucleotide reductase intermediate X. *J. Inorg. Biochem.* **100,** 771–779

16. Mitić, N., Clay, M. D., Saleh, L., Bollinger, J. M., Jr., and Solomon, E. I. (2007) Spectroscopic and electronic structure studies of intermediate X in ribonucleotide reductase R2 and two variants. A description of the FeIV-oxo bond in the FeIII-O-FeIV dimer. *J. Am. Chem. Soc.* **129,** 9049–9065

17. Burdi, D. W., Willems, J. P., Riggs-Gelasco, P., Antholine, W. E., Stubbe, J., and Hoffman, B. M. (1998) The core structure of X generated in the assembly of the di-iron cluster of ribonucleotide reductase. $^{17}O_2$ and $H_2^{17}O$ ENDOR. *J. Am. Chem. Soc.* **120,** 12910–12919

18. Reece, S. Y., Hodgkiss, J. M., Stubbe, J., and Nocera, D. G. (2006) Proton-coupled electron transfer. The mechanistic underpinning for radical transport and catalysis in biology. *Philos. Trans. R. Soc. Lond. B Biol. Sci.* **361,** 1351–1364

19. Adrait, A., Ohrström, M., Barra, A. L., Thelander, L., and Gräslund, A. (2002) EPR studies on a stable sulfinyl radical observed in the iron-oxygen-reconstituted Y177F/I263C protein R2 double mutant of ribonucleotide reductase from mouse. *Biochemistry* **41,** 6510–6516

20. Licht, S., Gerfen, G. J., and Stubbe, J. (1996) Thiyl radicals in ribonucleotide reductases. *Science* **271,** 477–481

21. Mao, S. S., Holler, T. P., Yu, G. X., Bollinger, J. M., Jr., Booker, S., Johnston, M. I., and Stubbe, J. (1992) A model for the role of multiple cysteine residues involved in ribonucleotide reduction. Amazing and still confusing. *Biochemistry* **31,** 9733–9743

22. Prinz, W. A., Aslund, F., Holmgren, A., and Beckwith, J. (1997) The role of the thioredoxin and glutaredoxin pathways in reducing protein disulfide bonds in the *Escherichia coli* cytoplasm. *J. Biol. Chem.* **272,** 15661–15667

23. Stubbe, J., and Riggs-Gelasco, P. (1998) Harnessing free radicals. Formation and function of the tyrosyl radical in ribonucleotide reductase. *Trends Biochem. Sci.* **23,** 438–443

24. Högbom, M., Stenmark, P., Voevodskaya, N., McClarty, G., Gräslund, A., and Nordlund, P. (2004) The radical site in chlamydial ribonucleotide reductase defines a new R2 subclass. *Science* **305,** 245–248

25. Voevodskaya, N., Lendzian, F., Ehrenberg, A., and Gräslund, A. (2007) High catalytic activity achieved with a mixed manganese-iron site in protein R2 of *Chlamydia* ribonucleotide reductase. *FEBS Lett.* **581,** 3351–3355

26. Boal, A. K., Cotruvo, J. A., Jr., Stubbe, J., and Rosenzweig, A. C. (2010) Structural basis for activation of class Ib ribonucleotide reductase. *Science* **329,** 1526–1530

27. Jiang, W., Yun, D., Saleh, L., Barr, E. W., Xing, G., Hoffart, L. M., Maslak, M. A., Krebs, C., and Bollinger, J. M., Jr. (2007) A manganese(IV)/iron(III) cofactor in *Chlamydia trachomatis* ribonucleotide reductase. *Science* **316,** 1188–1191

28. Bollinger, J. M., Jr., Jiang, W., Green, M. T., and Krebs, C. (2008) The manganese(IV)/iron(III) cofactor of *Chlamydia trachomatis* ribonucleotide reductase. Structure, assembly, radical initiation, and evolution. *Curr. Opin. Struct. Biol.* **18,** 650–657

29. Voevodskaya, N., Lendzian, F., Sanganas, O., Grundmeier, A., Gräslund, A., and Haumann, M. (2009) Redox intermediates of the Mn-Fe site in subunit R2 of *Chlamydia trachomatis* ribonucleotide reductase. An x-ray absorption and EPR study. *J. Biol. Chem.* **284,** 4555–4566

30. Leidel, N., Popović-Bijelić, A., Havelius, K. G., Chernev, P., Voevodskaya, N., Gräslund, A., and Haumann, M. (2012) High-valent [MnFe] and [FeFe] cofactors in ribonucleotide reductases. *Biochim. Biophys. Acta* **1817,** 430–444

31. Voevodskaya, N., Lendzian, F., and Gräslund, A. (2005) A stable FeIII-FeIV replacement of tyrosyl radical in a class I ribonucleotide reductase. *Biochem. Biophys. Res. Commun.* **330,** 1213–1216

32. Voevodskaya, N., Galander, M., Högbom, M., Stenmark, P., McClarty, G., Gräslund, A., and Lendzian, F. (2007) Structure of the high-valent FeIIIFeIV state in ribonucleotide reductase (RNR) of *Chlamydia trachomatis*. Combined EPR, ^{57}Fe-, ^{1}H-ENDOR and x-ray studies. *Biochim. Biophys. Acta* **1774,** 1254–1263

33. Schenk, G., Boutchard, C. L., Carrington, L. E., Noble, C. J., Moubaraki, B., Murray, K. S., de Jersey, J., Hanson, G. R., and Hamilton, S. (2001) A purple acid phosphatase from sweet potato contains an antiferromagnetically coupled binuclear Fe-Mn center. *J. Biol. Chem.* **276,** 19084–19088

34. Andersson, C. S., and Högbom, M. (2009) A *Mycobacterium tuberculosis* ligand-binding Mn/Fe protein reveals a new cofactor in a remodeled R2-protein scaffold. *Proc. Natl. Acad. Sci. U.S.A.* **106,** 5633–5638

35. Högbom, M. (2011) Metal use in ribonucleotide reductase R2, di-iron,

di-manganese and heterodinuclear. An intricate bioinorganic workaround to use different metals for the same reaction. *Metallomics* **3,** 110–120

36. Cotruvo, J. A., Jr., and Stubbe, J. (2012) Metallation and mismetallation of iron and manganese proteins *in vitro* and *in vivo*. The class I ribonucleotide reductases as a case study. *Metallomics* **4,** 1020–1036

37. Boal, A. K., Cotruvo, J. A., Jr., Stubbe, J., and Rosenzweig, A. C. (2012) The dimanganese(II) site of *Bacillus subtilis* class Ib ribonucleotide reductase. *Biochemistry* **51,** 3861–3871

38. Cotruvo, J. A., Jr., and Stubbe, J. (2010) An active dimanganese(III)-tyrosyl radical cofactor in *Escherichia coli* class Ib ribonucleotide reductase. *Biochemistry* **49,** 1297–1309

39. Cox, N., Ogata, H., Stolle, P., Reijerse, E., Auling, G., and Lubitz, W. (2010) A tyrosyl-dimanganese coupled spin system is the native metalloradical cofactor of the R2F subunit of the ribonucleotide reductase of *Corynebacterium ammoniagenes*. *J. Am. Chem. Soc.* **132,** 11197–11213

40. Lambertz, C., Leidel, N., Havelius, K. G., Noth, J., Chernev, P., Winkler, M., Happe, T., and Haumann, M. (2011) O₂ reactions at the six-iron active site (H-cluster) in [FeFe]-hydrogenase. *J. Biol. Chem.* **286,** 40614–40623

41. Andersson, C. S., Öhrström, M., Popović-Bijelić, A., Gräslund, A., Stenmark, P., and Högbom, M. (2012) The manganese ion of the heterodinuclear Mn/Fe cofactor in *Chlamydia trachomatis* ribonucleotide reductase R2c is located at metal position 1. *J. Am. Chem. Soc.* **134,** 123–125

42. Dassama, L. M., Boal, A. K., Krebs, C., Rosenzweig, A. C., and Bollinger, J. M., Jr. (2012) Evidence that the beta subunit of *Chlamydia trachomatis* ribonucleotide reductase is active with the manganese ion of its manganese(IV)/iron(III) cofactor in site 1. *J. Am. Chem. Soc.* **134,** 2520–2523

43. Que, L., Jr., and Tolman, W. B. (2002) Bis(mu-oxo)dimetal "diamond" cores in copper and iron complexes relevant to biocatalysis. *Angew. Chem. Int. Ed. Engl.* **41,** 1114–1137

44. Roos, K., and Siegbahn, P. E. (2011) Oxygen cleavage with manganese and iron in ribonucleotide reductase from *Chlamydia trachomatis*. *J. Biol. Inorg. Chem.* **16,** 553–565

45. Griese, J. J., and Högbom, M. (2012) X-ray reduction correlates with soaking accessibility as judged from four non-crystallographically related diiron sites. *Metallomics* **4,** 894–898

46. Garman, E. F. (2010) Radiation damage in macromolecular crystallography. What is it and why should we care? *Acta Crystallogr. D Biol. Crystallogr.* **66,** 339–351

47. Holton, J. M. (2009) A beginner's guide to radiation damage. *J. Synchrotron Radiat.* **16,** 133–142

48. Sommerhalter, M., Lieberman, R. L., and Rosenzweig, A. C. (2005) X-ray crystallography and biological metal centers. Is seeing believing? *Inorg. Chem.* **44,** 770–778

49. Högbom, M., Huque, Y., Sjöberg, B. M., and Nordlund, P. (2002) Crystal structure of the di-iron/radical protein of ribonucleotide reductase from *Corynebacterium ammoniagenes*. *Biochemistry* **41,** 1381–1389

50. Lindqvist, Y., Huang, W., Schneider, G., and Shanklin, J. (1996) Crystal structure of δ(9) stearoyl-acyl carrier protein desaturase from castor seed and its relationship to other di-iron proteins. *EMBO J.* **15,** 4081–4092

51. Logan, D. T., Su, X. D., Aberg, A., Regnström, K., Hajdu, J., Eklund, H., and Nordlund, P. (1996) Crystal structure of reduced protein R2 of ribonucleotide reductase. The structural basis for oxygen activation at a dinuclear iron site. *Structure* **4,** 1053–1064

52. Schlichting, I., Berendzen, J., Chu, K., Stock, A. M., Maves, S. A., Benson, D. E., Sweet, R. M., Ringe, D., Petsko, G. A., and Sligar, S. G. (2000) The catalytic pathway of cytochrome P450cam at atomic resolution. *Science* **287,** 1615–1622

53. Berglund, G. I., Carlsson, G. H., Smith, A. T., Szöke, H., Henriksen, A., and Hajdu, J. (2002) The catalytic pathway of horseradish peroxidase at high resolution. *Nature* **417,** 463–468

54. Adam, V., Royant, A., Nivière, V., Molina-Heredia, F. P., and Bourgeois, D. (2004) Structure of superoxide reductase bound to ferrocyanide and active site expansion upon x-ray-induced photoreduction. *Structure* **12,** 1729–1740

55. Wuerges, J., Lee, J. W., Yim, Y. I., Yim, H. S., Kang, S. O., and Djinovic

Carugo, K. (2004) Crystal structure of nickel-containing superoxide dismutase reveals another type of active site. *Proc. Natl. Acad. Sci. U.S.A.* **101,** 8569–8574

56. Kühnel, K., Jarchau, T., Wolf, E., Schlichting, I., Walter, U., Wittinghofer, A., and Strelkov, S. V. (2004) The VASP tetramerization domain is a right-handed coiled coil based on a 15-residue repeat. *Proc. Natl. Acad. Sci. U.S.A.* **101,** 17027–17032

57. Hough, M. A., Antonyuk, S. V., Strange, R. W., Eady, R. R., and Hasnain, S. S. (2008) Crystallography with online optical and x-ray absorption spectroscopies demonstrates an ordered mechanism in copper nitrite reductase. *J. Mol. Biol.* **378,** 353–361

58. Yano, J., Kern, J., Irrgang, K. D., Latimer, M. J., Bergmann, U., Glatzel, P., Pushkar, Y., Biesiadka, J., Loll, B., Sauer, K., Messinger, J., Zouni, A., and Yachandra, V. K. (2005) X-ray damage to the Mn₄Ca complex in single crystals of photosystem II. A case study for metalloprotein crystallography. *Proc. Natl. Acad. Sci. U.S.A.* **102,** 12047–12052

59. Haumann, M., Liebisch, P., Müller, C., Barra, M., Grabolle, M., and Dau, H. (2005) Photosynthetic O₂ formation tracked by time-resolved x-ray experiments. *Science* **310,** 1019–1021

60. Grabolle, M., Haumann, M., Müller, C., Liebisch, P., and Dau, H. (2006) Rapid loss of structural motifs in the manganese complex of oxygenic photosynthesis by x-ray irradiation at 10–300 K. *J. Biol. Chem.* **281,** 4580–4588

61. Yi, J., Orville, A. M., Skinner, J. M., Skinner, M. J., and Richter-Addo, G. B. (2010) Synchrotron X-ray-induced photoreduction of ferric myoglobin nitrite crystals gives the ferrous derivative with retention of the O-bonded nitrite ligand. *Biochemistry* **49,** 5969–5971

62. Purwar, N., McGarry, J. M., Kostera, J., Pacheco, A. A., and Schmidt, M. (2011) Interaction of nitric oxide with catalase. Structural and kinetic analysis. *Biochemistry* **50,** 4491–4503

63. Dau, H., and Haumann, M. (2008) The manganese complex of photosystem II in its reaction cycle. Basic framework and possible realization at the atomic level. *Coord. Chem. Rev.* **252,** 273–295

64. Cotelesage, J. J., Pushie, M. J., Grochulski, P., Pickering, I. J., and George, G. N. (2012) Metalloprotein active site structure determination. Synergy between X-ray absorption spectroscopy and X-ray crystallography. *J. Inorg. Biochem.* **115,** 127–137

65. Shi, W., and Chance, M. R. (2011) Metalloproteomics. Forward and reverse approaches in metalloprotein structural and functional characterization. *Curr. Opin. Chem. Biol.* **15,** 144–148

66. Younker, J. M., Krest, C. M., Jiang, W., Krebs, C., Bollinger, J. M., Jr., and Green, M. T. (2008) Structural analysis of the Mn(IV)/Fe(III) cofactor of *Chlamydia trachomatis* ribonucleotide reductase by extended x-ray absorption fine structure spectroscopy and density functional theory calculations. *J. Am. Chem. Soc.* **130,** 15022–15027

67. Riggs-Gelasco, P. J., Shu, L. J., Chen, S. X., Burdi, D., Huynh, B. H., Que, L., and Stubbe, J. (1998) EXAFS characterization of the intermediate X generated during the assembly of the *Escherichia coli* ribonucleotide reductase R2 diferric tyrosyl radical cofactor. *J. Am. Chem. Soc.* **120,** 849–860

68. Baldwin, J., Krebs, C., Saleh, L., Stelling, M., Huynh, B. H., Bollinger, J. M., Jr., and Riggs-Gelasco, P. (2003) Structural characterization of the peroxodiiron(III) intermediate generated during oxygen activation by the W48A/D84E variant of ribonucleotide reductase protein R2 from *Escherichia coli*. *Biochemistry* **42,** 13269–13279

69. Petrie, S., Gatt, P., Stranger, R., and Pace, R. J. (2012) Modelling the metal atom positions of the photosystem II water oxidising complex. A density functional theory appraisal of the 1.9-Å resolution crystal structure. *Phys. Chem. Chem. Phys.* **14,** 11333–11343

70. Grundmeier, A., and Dau, H. (2012) Structural models of the manganese complex of photosystem II and mechanistic implications. *Biochim. Biophys. Acta* **1817,** 88–105

71. Popović-Bijelić, A., Voevodskaya, N., Domkin, V., Thelander, L., and Gräslund, A. (2009) Metal binding and activity of ribonucleotide reductase protein R2 mutants. Conditions for formation of the mixed manganese-iron cofactor. *Biochemistry* **48,** 6532–6539

72. Klockenkämper, R. (1996) *Total Reflection X-ray Fluorescence Analysis*, Wiley-VCH, London, UK

73. Stripp, S., Sanganas, O., Happe, T., and Haumann, M. (2009) The structure of the active site H-cluster of [FeFe] hydrogenase from the green alga *Chlamydomonas reinhardtii* studied by x-ray absorption spectroscopy. *Biochemistry* **48,** 5042–5049

74. Haumann, M., Müller, C., Liebisch, P., Iuzzolino, L., Dittmer, J., Grabolle, M., Neisius, T., Meyer-Klaucke, W., and Dau, H. (2005) Structural and oxidation state changes of the photosystem II manganese complex in four transitions of the water oxidation cycle (S0 → S1, S1 → S2, S2 → S3, and S3,4 → S0) characterized by x-ray absorption spectroscopy at 20 K and room temperature. *Biochemistry* **44,** 1894–1908

75. Dau, H., Liebisch, P., and Haumann, M. (2003) X-ray absorption spectroscopy to analyze nuclear geometry and electronic structure of biological metal centers. Potential and questions examined with special focus on the tetra-nuclear manganese complex of oxygenic photosynthesis. *Anal. Bioanal. Chem.* **376,** 562–583

76. Zabinsky, S. I., Rehr, J. J., Ankudinov, A. L., Albers, R. C., and Eller, M. J. (1995) Multiple-scattering calculations of x-ray absorption spectra. *Phys. Rev. B* **52,** 2995–3009

77. Rehr, J. J. (2006) Theory and calculations of X-ray spectra. XAS, XES, XRS, and NRIXS. *Radiat. Phys. Chem.* **75,** 1547–1558

78. Liu, W. T., and Thorp, H. H. (1993) Bond valence sum analysis of metal-ligand bond lengths in metalloenzymes and model complexes. 2. Refined distances and other enzymes. *Inorg. Chem.* **32,** 4102–4105

79. Neese, F. (2008) *ORCA. An ab initio, DFT, and semiempirical electronic structure package version 2.6.35.* Theoretical Chemistry Group, Max-Planck Institute for Chemical Energy Conversion, Mühlheim, Germany

80. Chernev, P., Zaharieva, I., Dau, H., and Haumann, M. (2011) Carboxylate shifts steer interquinone electron transfer in photosynthesis. *J. Biol. Chem.* **286,** 5368–5374

81. Becke, A. D. (1988) Density-functional exchange-energy approximation with correct asymptotic behavior. *Phys. Rev. A* **38,** 3098–3100

82. Schäfer, A., Huber, C., and Ahlrichs, R. (1994) Fully optimized contracted Gaussian basis sets of triple ζ valence quality for atoms Li to Kr. *J. Chem. Phys.* **100,** 5829–5835

83. Weigend, F. (2006) Accurate Coulomb-fitting basis sets for H to Rn. *Phys. Chem. Chem. Phys.* **8,** 1057–1065

84. Sinnecker, S., Rajendran, A., Klamt, A., Diedenhofen, M., and Neese, F. (2006) Calculation of solvent shifts on electronic g-tensors with the conductor-like screening model (COSMO) and its self-consistent generalization to real solvents (Direct COSMO-RS). *J. Phys. Chem. A* **110,** 2235–2245

85. Seal, P., and Chakrabarti, S. (2008) Magnetic interactions in alkyl substituted cyclohexane diradical systems. A broken symmetry approach. *J. Phys. Chem. A* **112,** 3409–3413

86. Sinnecker, S., Neese, F., Noodleman, L., and Lubitz, W. (2004) Calculating the electron paramagnetic resonance parameters of exchange coupled transition metal complexes using broken symmetry density functional theory. Application to a Mn-III/Mn-IV model compound. *J. Am. Chem. Soc.* **126,** 2613–2622

87. Zwart, P. H., and Lamzin, V. S. (2003) Distance distributions and electron density characteristics of protein models. *Acta Crystallogr. D Biol. Crystallogr.* **59,** 2104–2113

88. Westre, T. E., Kennepohl, P., DeWitt, J. G., Hedman, B., Hodgson, K. O., and Solomon, E. I. (1997) A multiplet analysis of Fe K-edge 1s → 3d pre-edge features of iron complexes. *J. Am. Chem. Soc.* **119,** 6297–6314

89. Visser, H., Anxolabéhère-Mallart, E., Bergmann, U., Glatzel, P., Robblee, J. H., Cramer, S. P., Girerd, J. J., Sauer, K., Klein, M. P., and Yachandra, V. K. (2001) Mn K-edge XANES and K, XES studies of two Mn-oxo binuclear complexes. Investigation of three different oxidation states relevant to the oxygen-evolving complex of photosystem II. *J. Am. Chem. Soc.* **123,** 7031–7039

90. Roos, K., and Siegbahn, P. E. (2009) Density functional theory study of the manganese-containing ribonucleotide reductase from *Chlamydia trachomatis.* Why manganese is needed in the active complex. *Biochemistry* **48,** 1878–1887

91. Han, W. G., Giammona, D. A., Bashford, D., and Noodleman, L. (2010) Density functional theory analysis of structure, energetics, and spectroscopy for the Mn-Fe active site of *Chlamydia trachomatis* ribonucleotide

92. reductase in four oxidation states. *Inorg. Chem.* **49,** 7266–7281

93. Beitlich, T., Kühnel, K., Schulze-Briese, C., Shoeman, R. L., and Schlichting, I. (2007) Cryoradiolytic reduction of crystalline heme proteins. Analysis by UV-Vis spectroscopy and x-ray crystallography. *J. Synchrotron Radiat.* **14,** 11–23

94. Dubois, L., Jacquamet, L., Pecaut, J., and Latour, J. M. (2006) X-ray photoreduction of a di(mu-oxo)Mn(III)Mn(IV) complex occurs at temperatures as low as 20 K. *Chem. Commun.* (*Camb.*) **43,** 4521–4523

95. de Serrano, V. S., Davis, M. F., Gaff, J. F., Zhang, Q., Chen, Z., D'Antonio, E. L., Bowden, E. F., Rose, R., and Franzen, S. (2010) X-ray structure of the metcyano form of dehaloperoxidase from *Amphitrite ornata.* Evidence for photoreductive dissociation of the iron-cyanide bond. *Acta Crystallogr. D Biol. Crystallogr.* **66,** 770–782

96. Kim, J. H., Kim, Y. K., and Kang, H. (2009) Proton transfer and H/D isotopic exchange of water molecules mediated by hydroxide ions on ice film surfaces. *J. Chem. Phys.* **131,** 044705

97. Chen, S. H. and Loong, C. K. (2006) Neutron scattering investigations of proton dynamics of water and hydroxyl species in confined geometries. *Nuclear Engineer. Technol.* **38,** 201–224

98. Rasaiah, J. C., Garde, S., and Hummer, G. (2008) Water in nonpolar confinement. From nanotubes to proteins and beyond. *Annu. Rev. Phys. Chem.* **59,** 713–740

99. Hermes, S., Bremm, O., Garczarek, F., Derrien, V., Liebisch, P., Loja, P., Sebban, P., Gerwert, K., and Haumann, M. (2006) A time-resolved iron-specific X-ray absorption experiment yields no evidence for an Fe^{2+} → Fe^{3+} transition during Q_A → Q_B electron transfer in the photosynthetic reaction center. *Biochemistry* **45,** 353–359

100. Högbom, M., Galander, M., Andersson, M., Kolberg, M., Hofbauer, W., Lassmann, G., Nordlund, P., and Lendzian, F. (2003) Displacement of the tyrosyl radical cofactor in ribonucleotide reductase obtained by single-crystal high-field EPR and 1.4-Å x-ray data. *Proc. Natl. Acad. Sci. U.S.A.* **100,** 3209–3214

101. Voegtli, W. C., Sommerhalter, M., Saleh, L., Baldwin, J., Bollinger, J. M., Jr., and Rosenzweig, A. C. (2003) Variable coordination geometries at the diiron(II) active site of ribonucleotide reductase R2. *J. Am. Chem. Soc.* **125,** 15822–15830

102. Leidel, N., Chernev, P., Havelius, K. G., Schwartz, L., Ott, S., and Haumann, M. (2012) Electronic structure of an [FeFe] hydrogenase model complex in solution revealed by x-ray absorption spectroscopy using narrow-band emission detection. *J. Am. Chem. Soc.* **134,** 14142–14157

103. Dau, H., and Zaharieva, I. (2009) Principles, efficiency, and blueprint character of solar-energy conversion in photosynthetic water oxidation. *Acc. Chem. Res.* **42,** 1861–1870

104. Vass, I., and Styring, S. (1991) pH-Dependent charge equilibria between tyrosine-D and the S states in photosystem II. Estimation of relative midpoint redox potentials. *Biochemistry* **30,** 830–839

105. Magnuson, A., Liebisch, P., Högblom, J., Anderlund, M. F., Lomoth, R., Meyer-Klaucke, W., Haumann, M., and Dau, H. (2006) Bridging-type changes facilitate successive oxidation steps at about 1 V in two binuclear manganese complexes. Implications for photosynthetic water oxidation. *J. Inorg. Biochem.* **100,** 1234–1243

106. Gonzalez, A., and Nave, C. (1994) Radiation damage in protein crystals at low temperature. *Acta Crystallogr. D Biol. Crystallogr.* **50,** 874–877

107. Macedo, S., Pechlaner, M., Schmid, W., Weik, M., Sato, K., Dennison, C., and Djinović-Carugo, K. (2009) Can soaked-in scavengers protect metalloprotein active sites from reduction during data collection? *J. Synchrotron Radiat.* **16,** 191–204

108. Umena, Y., Kawakami, K., Shen, J. R., and Kamiya, N. (2011) Crystal structure of oxygen-evolving photosystem II at a resolution of 1.9 Å. *Nature* **473,** 55–60

109. Schlichting, I., and Miao, J. (2012) Emerging opportunities in structural biology with x-ray free-electron lasers. *Curr. Opin. Struct. Biol.* **22,** 613–626

110. Neutze, R., and Moffat, K. (2012) Time-resolved structural studies at synchrotrons and x-ray free electron lasers. Opportunities and challenges. *Curr. Opin. Struct. Biol.* **22,** 651–659

111. Fromme, P., and Spence, J. C. (2011) Femtosecond nanocrystallography using x-ray lasers for membrane protein structure determination. *Curr.*

Opin. Struct. Biol. **21,** 509 –516

111. Chapman, H. N., Fromme, P., Barty, A., White, T. A., Kirian, R. A., Aquila, A., Hunter, M. S., Schulz, J., DePonte, D. P., Weierstall, U., Doak, R. B., Maia, F. R., Martin, A. V., Schlichting, I., Lomb, L., Coppola, N., Shoeman, R. L., Epp, S. W., Hartmann, R., Rolles, D., Rudenko, A., Foucar, L., Kimmel, N., Weidenspointner, G., Holl, P., Liang, M., Barthelmess, M., Caleman, C., Boutet, S., Bogan, M. J., Krzywinski, J., Bostedt, C., Bajt, S., Gumprecht, L., Rudek, B., Erk, B., Schmidt, C., Hömke, A., Reich, C., Pietschner, D., Strüder, L., Hauser, G., Gorke, H., Ullrich, J., Herrmann, S., Schaller, G., Schopper, F., Soltau, H., Kühnel, K. U., Messerschmidt, M., Bozek, J. D., Hau-Riege, S. P., Frank, M., Hampton, C. Y., Sierra, R. G., Starodub, D., Williams, G. J., Hajdu, J., Timneanu, N., Seibert, M. M., Andreasson, J., Rocker, A., Jonsson, O., Svenda, M., Stern, S., Nass, K., Andritschke, R., Schroter, C. D., Krasniqi, F., Bott, M., Schmidt, K. E., Wang, X., Grotjohann, I., Holton, J. M., Barends, T. R., Neutze, R., Marchesini, S., Fromme, R., Schorb, S., Rupp, D., Adolph, M., Gorkhover, T., Andersson, I., Hirsemann, H., Potdevin, G., Graafsma, H., Nilsson, B., and Spence, J. C. (2011) Femtosecond x-ray protein nanocrystallography. *Nature* **470,** 73–77

112. Kern, J., Alonso-Mori, R., Hellmich, J., Tran, R., Hattne, J., Laksmono, H., Glöckner, C., Echols, N., Sierra, R. G., Sellberg, J., Lassalle-Kaiser, B., Gildea, R. J., Glatzel, P., Grosse-Kunstleve, R. W., Latimer, M. J., McQueen, T. A., DiFiore, D., Fry, A. R., Messerschmidt, M., Miahnahri, A., Schafer, D. W., Seibert, M. M., Sokaras, D., Weng, T. C., Zwart, P. H., White, W. E., Adams, P. D., Bogan, M. J., Boutet, S., Williams, G. J., Messinger, J., Sauter, N. K., Zouni, A., Bergmann, U., Yano, J., and Yachandra, V. K. (2012) Room temperature femtosecond x-ray diffraction of photosystem II microcrystals. *Proc. Natl. Acad. Sci. U.S.A.* **109,** 9721–9726

113. Boutet, S., Lomb, L., Williams, G. J., Barends, T. R., Aquila, A., Doak, R. B., Weierstall, U., DePonte, D. P., Steinbrener, J., Shoeman, R. L., Messerschmidt, M., Barty, A., White, T. A., Kassemeyer, S., Kirian, R. A., Seibert, M. M., Montanez, P. A., Kenney, C., Herbst, R., Hart, P., Pines, J., Haller, G., Gruner, S. M., Philipp, H. T., Tate, M. W., Hromalik, M., Koerner, L. J., van Bakel, N., Morse, J., Ghonsalves, W., Arnlund, D., Bogan, M. J., Caleman, C., Fromme, R., Hampton, C. Y., Hunter, M. S., Johansson, L. C., Katona, G., Kupitz, C., Liang, M., Martin, A. V., Nass, K., Redecke, L., Stellato, F., Timneanu, N., Wang, D., Zatsepin, N. A., Schafer, D., Defever, J., Neutze, R., Fromme, P., Spence, J. C., Chapman, H. N., and Schlichting, I. (2012) High-resolution protein structure determination by serial femtosecond crystallography. *Science* **337,** 362–364

114. Danford, J. J., Dobrowolski, P., and Berreau, L. M. (2009) Thioester hydrolysis reactivity of an Fe(III)Zn(II) complex. *Inorg. Chem.* **48,** 11352–11361

115. Lomoth, R., Huang, P., Zheng, J., Sun, L., Hammarström, L., Akermark, B., and Styring, S. (2002) Synthesis and characterization of a dinuclear manganese(III,III) complex with three phenolate ligands. *Eur. J. Inorg. Chem.* **2002,** 2965–2974